Polymer 253 (2022) 124901

Contents lists available at ScienceDirect

Polymer

journal homepage: www.elsevier.com/locate/polymer

# An experimentally validated model for quiescent multiphase primary and secondary crystallization phenomena in PP with low content of ethylene comonomer

Harm J.M. Caelers [a,*], Anke de Cock [a,**], Stan F.S.P. Looijmans [c], Ralf Kleppinger [a,b], Enrico M. Troisi [a], Martin van Drongelen [d], Gerrit W.M. Peters [c]

[a] SABIC, Technology and Innovation, 6167RD, Geleen, the Netherlands
[b] DSM, Materials Science, 6160BB, Geleen, the Netherlands
[c] Polymer Technology, Department of Mechanical Engineering, Eindhoven University of Technology, P.O. Box 513, 5600, MB Eindhoven, the Netherlands
[d] Faculty of Engineering and Technology, University of Twente, 7500AE, Enschede, the Netherlands

ARTICLE INFO

*Keywords:*
Structure and morphology
Propylene-ethylene random copolymer
Crystallization model
Polymorphism
Primary and secondary crystallization
Optical microscopy
Calorimetry
Synchrotron radiation

ABSTRACT

While crystallization behavior of isotactic polypropylene homopolymers had been subject to a wide range of experimental and modeling studies, this is not the case for propylene-ethylene random copolymers (PPR). This class of polymers offers up to now significant challenges, both from an experimental as well as a modeling perspective. The ethylene incorporation in the propylene chains, as well as the distribution of this comonomer, has a marked effect on the crystallization kinetics. Moreover, the presence of these defects causes a clear separation between primary crystallization (i.e. space filling) and subsequent secondary crystallization (increase of crystallinity in filled space) within the spherulitic skeletons, particularly subsequent at high primary crystallization temperatures. In this work, the underlying mechanism is first quantified by means of a combination of in-situ WAXD and SAXS experiments, as well as ex-situ WAXD experiments and calorimetric measurements. Based on these experiments an extended model framework is presented, capable of predicting multiphase non-isothermal crystallization kinetics as well as the final crystallinity as a function of the applied thermal conditions relevant for processing. The chemical composition distribution (CCD) of the ethylene comonomer serves as critical input to parameterize the model. Optical microscopy- and DSC experiments are used for parameterization of the primary crystallization model. The model developed in this study is, in principle, applicable to all polypropylenes, ranging from homo-polymers to random copolymers with variable comonomer content and/or CCD but, so far, only applied and validated on one PPR. To validate the model and the parameters for a given PPR, several non-isothermal and isothermal experiments (the latter followed by subsequent cooling) are conducted over a wide range of crystallization temperatures and cooling rates. The good match between experiments and model predictions demonstrates the power of the newly developed framework. The final crystallinity, the amount of $\alpha$- and $\gamma$-phase, and the ratio between primary and secondary crystallization can be predicted as a function of the time-temperature history. To the best knowledge of the authors, it is the first time that such a direct connection with the CCD is incorporated in a crystallization model. Consequently, the model offers a new tool to bridge the gap between chemical structure and resulting product properties, which now has come one step closer for PPR systems.

## 1. Introduction

Due to its versatile properties and low manufacturing costs, isotactic polypropylene (iPP) is one of the most widely used polymers after the invention of the catalytic process by Ziegler and Natta [1,2]. Today, with a grown interest on recyclability, it is expected that polyolefins in general, and more specific PP, will grow in importance even further. Therefore, continuous efforts are being made to close the gaps from

* Corresponding author.
** Corresponding author.
*E-mail addresses:* Harm.Caelers@SABIC.com (H.J.M. Caelers), Anke.Decock@SABIC.com (A. de Cock).

https://doi.org/10.1016/j.polymer.2022.124901
Received 1 February 2022; Received in revised form 26 April 2022; Accepted 27 April 2022
Available online 17 May 2022

chemical composition and processing conditions to material properties, in both academia and in industry [3–7]. Certain molecular structures give rise to the development of morphologies that are beneficial for specific desired properties. However, final product properties follow from the morphology, which is always resulting from a combination of the material characteristics at one hand, and the way it is shaped (i.e. thermo-mechanical history) into a product on the other [4,8].

The enormous versatility of properties that can be obtained within polypropylene materials arises to a large extent from its unique crystallization behavior, marked by polymorphism [9–13]. Bridging the gaps between molecular structure (molecular properties), processing conditions, morphology development and product properties (macroscopic) is an extremely challenging task, particularly for semi-crystalline materials. When considering isotactic polypropylene, solidified under moderate cooling conditions, predominantly monoclinic $\alpha$-phase crystals are observed. However, upon fast cooling a mesomorphic phase is formed [14]. This is a disordered crystalline form which has positional order only, and therefore, has features intermediate to amorphous phase and the other crystal forms [15]. In addition to these two phases, orthorhombic $\gamma$-phase [16] develops in isotactic iPP under high pressure [17,18]. Moreover, $\gamma$-crystals can develop at ambient pressures when low molecular weight iPP crystallizes. Besides the cooling rate and pressure applied during solidification, the chemical composition of the PP affects the competition between these phases as well [19]. With increasing defect content like reduced isotacticity or increased amount of comonomer [20–22], $\gamma$-phase formation is stimulated. Finally, pseudo-hexagonal $\beta$-phase [23] develops with the addition of a specific nucleating agent [24] or when crystallization takes place at high temperatures under certain flow conditions [25]. Besides polymorphism, both affected by the chemical composition and quiescent processing conditions, flow has a marked effect on crystallization and properties [8,26,27]. Although flow is not in the scope of the current study, several authors have extensively studied these phenomena [28–31].

In contrast to iPP, PPR like the ethylene propylene copolymer used in this work, displays a more rich polymorphism in ambient quiescent conditions. Moreover, ethylene defects can be incorporated into the crystal lattice and affect the crystal density, lattice dimensions and thermal behavior [32–35]. Due to the effects this exerts on the mechanical performance, PPR's are important materials that add additional options to the already versatile properties, available from iPP. Despite the complex crystallization behavior of iPP, the group of Peters recently managed to model multiphase multimorphology crystallization behavior of iPP [8,28,36]. The strength of this model framework is its applicability to a variety of semi-crystalline materials, as was demonstrated and validated in several publications. So far, owing to its chemical heterogeneity PPR copolymer is not yet modeled in the aforementioned framework. In comparison to iPP, PPR has larg fractions of material that cannot unconditionally participate in the crystallization process at high temperatures, which can result in large portions of secondary crystallization [37].

A thorough understanding of the crystallization behavior allows to adequately steer material development, as well as processing conditions in production steps, in order to obtain desired macroscopic properties. Due to the high amount of parameters affecting the crystallization kinetics, influenced by molecular features and locally variable conditions experienced during and prior to solidification in real-life processing, a decent crystallization model allowing to study the influence of separate parameters is of vital importance. Predictive capability will boost material development, increase efficiency and reduce experimental costs.

The aim of this study is to develop an experimentally validated crystallization model, applicable to PPR, which can be adopted for different amounts and types of comonomer, by varying the input parameters. Moreover, the model should be applicable to several thermal histories, ranging from processing relevant cooling rates to isothermal crystallization. First, PPR crystallization phenomena are treated to illustrate similarities with iPP, and subsequently, some characteristics that are specifically evident in PPR will be discussed. After the crystallization phenomena of PPR are treated, a model approach is introduced, parameterized and validated with optical microscopy, thermal analyses techniques and in-situ X-ray experiments.

## 2. Crystallization phenomena in PP random copolymers

The majority of the crystallization studies carried out on PPR focused on measuring and understanding the results of the complex crystallization behavior of these materials, rather than modeling the kinetics and, with that, predict these results. These studies give important insights to be accounted for when developing a model framework for PPR. Below, the key phenomena that are typical for PP crystallization in general, and more specifically for PPR, are treated further.

### 2.1. Multi-phase crystallization at ambient pressure

As explained in the introduction, polypropylene can adopt several unit cell structures when crystallizing. If highly isotactic homopolymers crystallize in the absence of $\beta$-specific nucleating agents in quiescent conditions, a competition between mesophase and $\alpha$-phase takes place [36,38]. Depending on the cooling rate and thus the crystallization temperature, either one of them dominates and in a specific temperature window between 40 and 50 $^{\circ}C$ a combination of the two is formed [39,40]. In the case of a random- or low molecular weight polypropylene, $\gamma$-phase can develop at ambient pressure, while in highly isotactic iPP, elevated pressures need to be applied in order to get $\gamma$-crystals [17,20]. With increasing comonomer content, an increase in the $\gamma$-fraction is observed [41–44]. Interestingly, $\alpha$- and $\gamma$-crystals form within the same spherulites [18,22,44–46], whereas $\beta$- and mesophase form separate spherulites and nodules, respectively [8,39,47]. In general it is accepted that $\gamma$-phase cross nucleates on $\alpha$ lamellae [44,48], meaning that in order to grow $\gamma$-crystals, $\alpha$ crystals must be formed first. Zhang et al. [18] revealed a mechanism of the formation of an $\alpha$-skeleton in which prevailing development of the $\gamma$-form takes place in iPP at elevated pressures. This is an important finding that will be used and explained further in section 3, as it affects the model framework. Several authors linked the maximum amount of $\gamma$ phase formation to the sequence length [41,45].

Besides the effect on the $\alpha$-$\gamma$- competition, the ethylene comonomer exerts an effect on the mesomorphic phase and the $\beta$-crystals as well. The higher the ethylene content, the more the $\beta$-phase formation is suppressed [49]. In processing, when ballistic cooling is applied, the increased ethylene content results in a decreased crystallization temperature window where mesophase is formed [38]. Nevertheless, besides $\alpha$- and $\gamma$-structures, the mesophase is the third important structure that forms in PPR's. The presence of the mesophase is accompanied with a consequence for the crystallization model in terms of the nucleation mechanism. It is well known that mesophase proceeds via a homogeneous nucleation mechanism [50–53], which is in contrast with the other crystals that form from a heterogeneous nucleation mechanism [51]. In polypropylene, heterogeneous nucleation (pre-existing or dormant nuclei) dominates crystallization at low under-cooling and is activated by lowering the temperature. Homogeneous nucleation, i.e. thermal size fluctuations of ordered domains surpassing a critical size, dominates nucleation at high under-cooling [38,51].

For an iPP homopolymer, multiphase crystallization kinetics are modeled successfully in Refs. [36,54]. The proposed framework is capable of predicting multiphase structure development in quiescent, non-isothermal conditions. For convenience, the nucleation mechanism of the mesophase was heterogeneous in that specific work, but can easily be exchanged for a homogeneous mechanism [55]. Notice that this modeling was successfully extended to include flow, i.e. to capture real life processing conditions [8,28].

### 2.2. Primary and secondary crystallization

In the work of Nozaki et al. [37], a clear distinction between primary and secondary crystallization phenomena was revealed. They found that primary isothermal crystallization of a PPR at a given (high) temperature results in a temperature dependent ratio between $\alpha$- and $\gamma$-crystallites. Additionally, even after reaching full spacefilling at isothermal conditions, the relatively low crystallinity increases upon subsequent cooling and the ratio $\gamma$-to $\alpha$-changes significantly. Both $\alpha$-$\alpha$ homo- or $\alpha$-$\gamma$ hetero-epitaxy are common, but the majority of the crystals formed in the subsequent cooling step adopts an orthorhombic $\gamma$-unit cell structure. The latter is a secondary crystallization phenomenon and can result from lamellar insertion or lamellar thickening. This observation has important consequences for the development of the model since in-situ measurements are required to split primary and secondary crystallization phenomena, and be able to quantify the behavior. Findings similar to Nozaki et al. were obtained by Auriemma et al. [56], who investigated melt crystallization of mixtures of regular and irregular isotactic polypropylene. Crystallization in well separated temperature ranges resulted in the formation of different populations of intermixed lamellar stacks. Crystallization induced phase separation starts at the onset of crystallization of the high stereoregular iPP component. Consequently, the concentration of the low stereoregular component in the non-crystalline surrounding increases further. Upon further cooling, the irregular component crystallizes and forms independent stacks of lamellae in the interlamellar amorphous regions. Combining the findings of Nozaki et al. with the findings of Auriemma et al. suggests that a similar mechanism could take place upon isothermal crystallization and subsequent cooling of PPR. At the relatively high isothermal crystallization temperatures, only a fraction will be able to crystallize. Given the ethylene content of this specific fraction, a certain ratio between $\alpha$- and $\gamma$-crystals will be formed. The resulting spherulites or skeletons have a rather open structure, composed of thick lamellae. Upon subsequent cooling, the second fraction with an increased ethylene content starts to crystallize. The change in ethylene content translates into the ratio $\alpha$-versus $\gamma$ crystals. Such a process also takes place in continuous cooling experiments, but since the differences between the ethylene containing fractions, present in commercial PPR's, are not as extreme as for example the materials used in the work of Auriemma et al., the consequences are less obvious. Nevertheless, ratio's between the various fractions can be utilized to steer morphology and thus mechanical properties [57].

Secondary crystallization phenomena like lamellar insertion are incorporated succesfully in models, for example by van Drongelen et al. [58] for LLDPE and by Yaghini and Peters for polyamide 6 [59]. However, the presence of polymorphism in PPR makes that the approach is not directly applicable.

### 2.3. Decreasing crystallinity with increasing crystallization temperature

In general, crystallization of semi-crystalline polymers results in higher crystallinities upon increasing crystallization temperatures, particularly when looking in the temperature regime in which crystallization occurs at accessible timescales. In PPR, contradicting findings have been reported. The heat of fusion, recorded during isothermal crystallization at several temperatures, displays a maximum [60]. With increasing amount of ethylene content this maximum enthalpy of fusion shifts towards lower temperatures [43], i.e. the temperature at which the maximum crystallinity is obtained, decreases with ethylene content. These results can be linked to the primary and secondary crystallization phenomena. It strongly suggests that in the case of a PPR (or another material with large stereo-irregularity), certain fractions are not able to crystallize at high temperatures. Only the highly isotactic fractions can adopt a crystalline structure under these conditions, whereas fractions with lower isotacticity or higher comonomer content tend to crystallize at lower temperatures, causing a progressively decreasing crystallinity towards the high temperature regime. Depending on the overall defect content, and the chemical composition distribution of these defects, the optimum isothermal crystallization temperature, i.e. the isothermal temperature that results in the highest crystallinity, is determined.

Recently, it was demonstrated that the maximum crystallinity can be predicted from a model framework, applied to polyamide 6 [59]. At infinite time, the maximum crystallinity is temperature dependent in this model, for which only a certain range of crystallization temperatures are considered. In the investigated temperature regime, the polyamide did not display a decrease in crystallinity with increasing crystallization temperature. This means that the approach to predict final crystallinity levels can only partially be adopted.

### 2.4. Heat of fusion

The heat of fusion is often used to determine the crystallinity. This approach is particularly useful in case of Flash DSC experiments (small amounts of sample on a chip makes it difficult to combine with X-ray) or in case X-ray is not available. However, in case of multiphase materials, it is difficult to obtain exact crystallinity levels. Each crystal phase has its own heat of fusion, meaning that information on the phase composition is required [33,34]. Moreover, upon heating, melting and recrystallization phenomena can occur in case the heating rate is not sufficiently high [40,61]. Additionally, in the specific case of PPR, a small portion of the ethylene present in the PPR can incorporate in the crystal lattice [32,62]. This gives a reduction in crystal density, but also decreases the melting enthalpy of the crystals and changes the dependency of $T_m$ with comonomer content [35]. The correct value of the enthalpy of fusion can best be determined by a combination of X-ray and DSC experiments, which unfortunately is often not available.

## 3. Model approach

In quiescent conditions, polymer crystallization from the melt is generally governed by two processes: nucleation and growth. From the nuclei, crystallites grow laterally with a temperature dependent thickness, the so-called lamellar thickness, which increases with crystallization temperature [63–66]. The growing lamellae are mostly ordered in spherulitic structures. If large enough, radial growth of these spherulites can macroscopically be observed and monitored over time by means of, for example, polarized optical light microscopy (POM). The temperature dependent primary growth rate, in combination with the number of spherulites, determines the rate of spacefilling, the point at which spherulites start to impinge and, consequently, when the radial growth stops. Even at full spacefilling, non-crystallized amorphous regions are left in between the lamellae. Where the spacefilling $\xi$ evolves form 0 (melt) to 1 (full spacefilling), the final crystallinity level $\chi$, which is defined as the fraction of crystals, is smaller, and for PP typically grows from 0 to values in between 0.4 and 0.65. This difference between $\xi$ and $\chi$ is a consequence of the semicrystalline nature of polypropylene, and both represent different features. In case part of the space is filled, two different crystallinity values can be distinct. The first one is the overall crystallinity and denotes the fraction of crystals in the total volume (filled and unfilled space). The second one is a local crystallinity and denotes the crystallinity within the filled space. At full space filling, the two equal to one another. In the remainder of this article, the local averages are referred to with superscripts, i.e. $\chi^a$, whereas the overall averages are referred to with subscripts: $\chi_a$.

### 3.1. Primary crystallization

In this work, crystallization that takes place at the front of growing spherulites during the spacefilling process is considered to be the primary crystallization.

We will first focus solely on primary crystallization, in which the spacefilling based on nucleation and unconfined three-dimensional

growth can be described using the Kolmogoroff Equation [67]:

$$\xi(t) = 1 - exp\left( - \sum_i \varphi_{0,i}(t) \right) \tag{1}$$

where $\varphi_{0,i}(t)$ is the undisturbed total volume of all spherulites of phase $i$ (i.e. impingement is disregarded), given by:

$$\varphi_{0,i}(t) = \frac{4\pi}{3} \int_{-\infty}^{t} dt^{'} N_i(t^{'}) \left[ \int_{-\infty}^{t} du G_i(u) \right]^3 \tag{2}$$

Experimentally, the spacefilling $\xi(t)$ can be extracted with, for example, in-situ X-ray measurements, provided that the secondary crystallization is negligible. By monitoring the overall average primary crystallinity at time $t$, $\chi_p(t)$ can be normalized with the maximum final primary crystallinity $\chi_{\infty,p}$ to obtain spacefilling. Additionally, spacefilling can be extracted from optical microscopy experiments. As will be demonstrated later, $\chi_{\infty,p}$ is not a constant, but a direct result of the thermo (-mechanical) history experienced during the primary crystallization process.

In Equation (2), the phase specific spherical nucleation density $N_i(t') = N_i(T(t'), p(t'))$ and growth rate $G_i(u) = G_i(T(u), p(u))$ are both temperature ($T$) and pressure ($p$) dependent. In the special case where both pressure and temperature are constant during crystallization, Equation (1) reduces to the well-known Avrami equation [68,69].

In this work, crystallization at non-isothermal conditions under ambient pressure is considered. The Schneider rate equations [70] translate Equation (2) into a set of more convenient differential equations:

$$\begin{aligned}
\frac{d\varphi_{3,i}}{dt} &= 8\pi \dot{N}_{i,k,q} \qquad (\varphi_3 = 8\pi N_i) \\
\frac{d\varphi_{2,i}}{dt} &= G_i \varphi_{3,i} \qquad (\varphi_2 = 8\pi R_{tot,i}) \\
\frac{d\varphi_{1,i}}{dt} &= G_i \varphi_{2,i} \qquad (\varphi_1 = S_{tot,i}) \\
\frac{d\varphi_{0,i}}{dt} &= G_i \varphi_{1,i} \qquad (\varphi_0 = V_{tot,i})
\end{aligned} \tag{3}$$

Equation (3) hold for spherulites and mesomorphic nodules, since in this work it is assumed that both structures grow spherically, rather than for example the disc like structures for polyamide 12 as described by Paolucci et al. [55]. Here, $\dot{N}_{i,k,q}$ is the nucleation rate of phase $i$, for quiescent conditions $q$. $k$ denotes the nucleation mechanism, either homogenous or heterogeneous. The total amount of nuclei $N$ grow radially with a growth rate $G$ into a total radius $R_{tot}$. Both, the total undisturbed volume $V_{tot}$ and the total spherulitic surface $S_{tot}$ can be extracted from the Schneider rate equations as well.

Upon primary crystallization, all crystal phases as well as the mesomorphic phase can be formed. While the mesophase typically forms in separated nodules [39,50,51], and the $\beta$-phase tends to form distinct $\beta$ spherulites [47], $\gamma$ co-crystallizes at the lamellar length scale into $\alpha$-based structures [18,22,44].

The space filling is therefore calculated by:

$$\xi = \sum_{n=\alpha,\beta,m} \xi_n \tag{4}$$

The rate of change of spacefilling of each individual crystal phase contributing to this process follows from:

$$\dot{\xi}_n = (1 - \xi)\dot{\varphi}_{0,n} \tag{5}$$

Note that gamma does not contribute to the spheruletic spacefilling process and, therefore, needs to be incorporated into the model in an alternative fashion. In the work of Looijmans et al. [71], a crystallization model for cross-nucleation is presented. This model is based on experimental observations of clear 'pie slices' of one phase, nucleating on a sperulitical structure of the other phase since the number of cross-nuclei is relatively low and growth rates are significantly different. In the present work, we also have a case of nucleation of $\gamma$ phase in/on the $\alpha$ crystals (hetero epitaxy), but less clearly separated and (most probably) at a lamellar scale [48]. Notice that, in the temperature regime where both the $\alpha$ and $\gamma$ phase grow, the growth rates are nearly the same. If the growth rates of both phases are nearly the same and proceed at the small local scale of the lammellae (high cross-nucleation densities), they show local fluctuations. The growth of one phase after cross nucleation can dominate for a period, but can later or elsewhere be overtaken by the other one [65]. This causes a mixture of the two phases, of which, at a constant temperature, the overall volume ratio is constant. Moreover, since clear pie slices are typically not observed (also not in this study), modeling of $\gamma$-growth based on the geometrical observations as suggested by Looijmans et al. does not apply here.

With these considerations in mind, we propose to follow the observations of Zhang et al., who reported the formation of an $\alpha$-skeleton in which $\gamma$- and $\alpha$ lamellae can grow. The volume ratio of the $\alpha$ and $\gamma$ phases is constant at a fixed temperature, and can be determined by attributing the radial spheruletic growth rate to $\alpha$-crystals. Hence $\alpha$ needs to grow before $\gamma$ grows. The space, occupied by $\alpha$ skeletons or mixed $\alpha$, $\gamma$ structures, is denoted with $\xi_\alpha$. Within this space, apparent space fillings, i.e. that do not count up to the total space filling, can be calculated. These apparent spaces $\xi_{\alpha\alpha}$ and $\xi_{\gamma\alpha}$ are obtained using

$$\xi_{\alpha\alpha} = \xi_\alpha \cdot \frac{\xi_\alpha}{\xi_\alpha + \xi_\gamma}; \qquad \xi_{\alpha\gamma} = \xi_\alpha \cdot \frac{\xi_\gamma}{\xi_\alpha + \xi_\gamma}; \qquad \xi_\alpha = \xi_{\alpha\alpha} + \xi_{\alpha\gamma} \tag{6}$$

and are calculated from $\xi_\alpha$ and $\xi_\gamma$, following from Equation (5). Note that $\xi_\gamma$ is an apparent space occupied by $\gamma$ crystals, growing with an apparent growth rate $G_\gamma$, and does not represent a physical volume. Therefore, in Equation (4) it is not accounted for $\gamma$-crystals. Nevertheless, $\xi_\gamma$ is calculated using equation (3). Since $\gamma$ grows into $\alpha$ spherulites, both have the same nucleation density $N_\alpha$. In conclusion, the above equations mean that after reaching full spacefilling, the following relations should hold:

$$\xi = \sum_{n=\alpha,\beta,m} \xi_n = \sum_{i=\alpha\alpha,\alpha\gamma,\beta,m} \xi_i = 1 \tag{7}$$

This approach implies that in the absence of $\beta$ and meso crystals, the radial growth rate observed in optical microscopy experiments, is controlled by- and attributed to the $\alpha$-phase. Alamo et al. report two growth rates extracted from optical microscopy experiments, executed during isothermal crystallization at various high temperatures of random polypropylenes with different comonomer content [22]. They explained this observation by the transition from mixed $\alpha$, $\gamma$ formation at the early stages of crystallization, to the growth of purely $\gamma$ at the growth front. Such a transition is expected only at large timescales and relatively high isothermal crystallization temperatures. Therefore, the assumption to assign the radial growth rate to $\alpha$ is expected to hold in case of crystallization at time scales below 100 min, and definitely in time scales typically assessed in industrial production processes.

The phase specific pressure and temperature dependent growth rates and nucleation rates are described by the expressions (8) and (9) respectively, similar to Ref. [36].

$$G_i(T,p) = G_{max,i}(p) exp(-c_{g,i}(T(t) - T_{Gref,i}(p))^2) \tag{8}$$

In this equation, $G_{max,i}$ is the maximum growth rate at reference temperature $T_{G,ref,i}$, of each crystal phase $i$. The width of the Gaussian shaped growth rates is given by the constants $c_{g,i}$. Even though the radial growth rate of $\gamma$-PP does not have a direct physical meaning since the $\gamma$-crystals co-crystallize, the model describes $\gamma$ crystallization with a unique apparent growth rate. In isothermal isobaric quiescent conditions, the growth rates should be constant. The nucleation mechanism is more straightforward. Mesophase results from a purely homogeneous nucleation rate while the other crystal phases originate from

heterogeneous nucleation. Since $\alpha$ and $\gamma$ co-crystallize, their nucleation rate is equal, see Equation (9). In the absence of flow or a $\beta$-specific nucleating agent, no $\beta$-crystals are expected to form and, therefore, this phase is not considered in this work.

$$\begin{aligned}\dot{N}_{\alpha,het,q}(T,p) &= \dot{N}_{\gamma,het,q}(T,p) = \dot{T}\frac{dN_{\alpha,het,q}}{dT} \\ \dot{N}_{m,hom,q}(T,p) &= \dot{N}_{m,hom,q}\end{aligned} \tag{9}$$

The $\alpha$-nucleation rate comprises the amount of nuclei as a function of the crystallization temperature, equation (10). By counting the amount of spherulites in different isothermal crystallization experiments, the heterogeneous nucleation rate for the $\alpha$-phase can be estimated.

$$\frac{dN_{\alpha,het,q}}{dT} = -c_n N_{ref} exp(-c_n(T(t) - T_{Nref}(p))) \tag{10}$$

Temperature dependent homogeneous nucleation rates of a mesophase can be described as for example done by Koutsky et al. and Paolucci et al. [55,72]. However, especially in the case of mesophase polypropylene, a significant number of the required parameters is either not reported in literature (to the knowledge of the authors), has limited physical meaning, or a variety of different values are reported. Therefore, it is chosen to describe the bell-shaped homogeneous nucleation rate $\dot{N}_{m,hom,q}$ with an equation equivalent to Equation (8). This function does not reproduce the typical non-symmetric shape of the homogeneous nucleation rate, but is chosen since it closely matches the curvature in the relevant temperature window, i.e. where the mesophase forms.

$$\dot{N}_{n,hom,q} = N_{max,h} exp(-c_{n,h}(T(t) - T_{Nref,h})^2) \tag{11}$$

So far, the focus has been on polymorphism and spacefilling, but what additionally determines the properties, is the fraction of the crystals and the thickness of the crystals [73,74]. Therefore, being predictive with respect to crystallinity is of added value to the model. Typically, the spacefilling needs to be multiplied with a final primary crystallinity level (of phase $i$) $\chi^p_{\infty,i}$, obtained in the filled space, in order to calculate a global crystallinity $\chi_{p,i}$. Here, it is suggested to use a temperature dependent local $\chi^p_{\infty,i}(T(t))$.

To obtain $\chi_{p,i}$, the crystallinity occurring at time $t_p$ at the front of growing crystalline structures of phase $i$, $\chi^p_{\infty,i}(t_p, \xi_{t_p,i})$ (with $i = \alpha\alpha$, $\beta$, $\alpha\gamma$, $m$) is integrated over the filled space. $\xi_{t_p,i}$ indicates the location of that crystallinity level, i.e. the filled space at time $t_p$ of phase $i$ (again, notice that we use superscript for local crystallinity while for volume averaged specific crystallinity we use subscript).

The specific primary crystallinity of phase $i$, i.e the primary crystallinity in a representative volume where the space filling takes place, is given by:

$$\chi_{p,i}(t,\xi_i) = \int_0^{\xi_i} \chi^p_{\infty,i}\left(t, \xi_{t_p,i}\right) d\xi_{t_p,i} \tag{12}$$

Equation (12) requires phase specific $\chi^p_{\infty,i}$ values, which is undesired, since this information is experimentally not accessible. Therefore, it as assumed that the final primary crystallinity level of all phases is equal, and equation (12) reduces to:

$$\chi_{p,i}(t,\xi_i) = \int_0^{\xi_i} \chi^p_{\infty}\left(t, \xi_{t_p,i}\right) d\xi_{t_p,i} \tag{13}$$

The total primary crystallinity, i.e. the sum over all phases, is given by:

$$\chi_p(t) = \sum\nolimits_{i=1}^{n} \chi_{p,i}(t,\xi_i) \tag{14}$$

### 3.2. Secondary crystallization

As soon as a certain volume is occupied with primary crystals, the crystallinity can locally grow further. This phenomenon, with the accompanying increase in crystallinity, is referred to as secondary crystallization and is enabled after primary crystals are formed, i.e. secondary crystallization can start in the filled areas, before complete spacefilling is reached. In PP random copolymer, secondary crystallization phenomena can significantly contribute to the crystallinity, depending on the thermal history applied during the solidification process [37]. Besides an increase in crystallinity, the phase composition can change due to phenomena like lamellar insertion or thickening (of different polymorphs). Similar secondary phenomena have been captured in a model by van Drongelen et al. [58] who investigated primary and secondary crystallization in LLDPE, using a convolution integral to capture the evolution in the maximum crystallinity. More recently, Yaghini and Peters modeled secondary crystallization of polyamide 6 [59]. To incorporate multiphase secondary crystallization in the model at hand, first a rather general model for multi-phase secondary crystallization will be presented. Next, to make the model applicable, some simplifications are introduced.

The local primary crystallinity $\chi^p_{\infty,i}$, formed in the primary crystallization step at the front of a growing spherulite, can further increase over time. The level of secondary crystallinity of a phase $j$, $j = \alpha$, $\beta$, $\gamma$, $m$, at time $t$, in all positions that were occupied at time $t_p$ by a growing primary semi-crystalline structure $i$, is given by:

$$\chi^s_{ij}\left(t, \xi_{t_p,j}\right) = \int_{t_p}^{t} \dot{\chi}^s_{ij}\left(T(t'), \xi_{t_p,j}\right) dt' \tag{15}$$

Again, it is emphasized that these are local crystallinity levels (i.e. in a given position in a spherulite) and not the crystalinity levels in a representative volume, i.e. a volume which contains multiple (growing) crystalline structures as, for example, spherulites.

If $i = j$, the secondary crystallizing phase is the same as the primary crystallizing phase, i.e. $\alpha$ crystallizes in $\alpha$. If $i \neq j$, the secondary phase is different from the primary one, e.g. $\gamma$ crystallizes in $\alpha$. Notice that different phases can grow as secondary structures simultaneously in the same primary crystallized phase.

The rate of change of the crystallinity at these positions $\xi_{t_p,j}$ for $t > t_p$, $\dot{\chi}_{ij}\left(\xi_{t_p,j}, T(t)\right) = \dot{\chi}^s_{ij}(T(t))$ is assumed to be a function of the temperature and the difference with the maximum secondary crystallinity level that can be obtained at a given temperature for isothermal conditions. Moreover, the initial condition is given by $\chi^s_{ij}\left(t_p, \xi_{t_p j}\right) = 0$.

The specific secondary crystallinity of phase $i$, i.e the secondary crystalinity in a representative volume occupied by phase $j$ in the primary process, is given by:

$$\begin{aligned}\chi_{s,ij}(t,\xi_j) &= \int_0^{\xi_j} \chi^s_{ij}\left(t, \xi_{t_p,j}\right) d\xi_{t_p,j} = \int_0^{\xi_j} \left[\int_0^{\xi_j} \dot{\chi}^s_{ij}\left(T(t'), \xi_{t_p,j}\right) dt'\right] d\xi_{t_p,j} \\ &= \int_0^{t} \left[\int_{t_p}^{t} \dot{\chi}^s_{ij}\left(T(t'), \xi_{t_p,j}\right) dt'\right] \dot{\xi}_j dt\end{aligned} \tag{16}$$

The total secondary crystallinity contributing to phase i is given by:

$$\chi_{s,i}(t) = \sum\nolimits_{j=1}^{p} \chi_{s,ij}(t,\xi_j) \tag{17}$$

In our case only the $\alpha$ and $\gamma$ phase are considered to grow during secondary crystallization processes, and thus, $j = \alpha$, $\gamma$. The total secondary crystallinity is given by:

$$\chi_s(t) = \sum\nolimits_{i=1}^{m} \chi_{s,i}(t) \tag{18}$$

Since in this work secondary crystalization is only considered in the $\alpha$ skeletons, and not in spaces occupied by $\beta$- and/or mesophase, $i = \alpha$ in equation (18).

Next, a constitutive equation describing the secondary crystallization behavior has to be specified. A phenomenological expression for the single phase case is given by van Drongelen et al., and Yaghini & Peters [58,59]:

$$\begin{aligned}\dot{\chi}^s\left(T,\xi_{t_p,i}\right) &= \left(\chi^s_\infty\left(T\left(t_p\right)\right)-\chi^s(t)\right)^n K(T)\\ &\chi^s_\infty-\chi^s(t)\geq 0\end{aligned} \tag{19}$$

where $\chi^s_\infty$ is maximum level that secondary crystallization can reach for isothermal conditions, i.e for the temperature at time $t_p$. In other words, the maximum level that secondary crystallization at positions defined by $\xi_{t_p}$ can reach, is determined by the temperature at that position at the moment it was occupied by the growing semi-crystalline structure. For any thermal history that does not include melting the term $\chi^s_\infty-\chi^s(t)$ is assumed to become zero when $\chi^s_{\infty,i}<\chi^s_i(t)$, i.e. $\chi^s(t)$ cannot decrease. The temperature depent rate function $K$ is given by:

$$K(T)=a\cdot exp\left(-b\frac{\left(T-T_{ref}\right)^2}{T^2}\right) \tag{20}$$

in which $T_{ref}$ represents the temperature for which the rate of secondary crystallization reaches its maximum $a$, and the parameter $b$ governs the width of the function $K(T)$. Generalizing this expression for a multiphase case can be done by specifying the temperature dependent secondary crystallization rate for each separate phase. Based on expression (19), such an extended version for the multi phase case looks like:

$$\begin{aligned}\dot{\chi}^s_{i,j}\left(T,\xi_{t_p,i}\right) &= \left(\chi^s_{\infty,i}\left(T\left(t_p\right)\right)-\chi^s_{ij}(t)\right)^n K_i(T)\\ &\chi^s_{\infty,i}-\chi^s_{ij}(t)\geq 0\end{aligned} \tag{21}$$

However, such a general approach requires a rather large number of parameters of which it is questionable if these can be determined with reasonable experimental effort, if possible at all. Therefore, a simplified constitutive equation for multiphase secondary crystallization is proposed in which one total value for the maximum secondary crystallization is used and the contribution to the different phases is expressed by the rate function $K_j(T)$:

$$\begin{aligned}\dot{\chi}^s_j\left(T,\xi_{t_p,i}\right) &= \left(\chi^s_\infty\left(T\left(t_p\right)\right)-\chi^s(t)\right)^n K_i(T)\\ &\chi^s_\infty-\chi^s(t)\geq 0\end{aligned} \tag{22}$$

In which $\chi^s(t)$ is the sum of the secondary crystallization of the different phases:

$$\chi^s(t)=\sum\nolimits_{j=1}^{n}\sum\nolimits_{i=1}^{n}\chi^s_{ij}(t) \tag{23}$$

For the random PP's considered here, the determination of the maximum level of secondary crystallization $\chi^s_\infty$ will be discussed in detail in the next section. Evaluating Equation (16) can be numerically demanding. An approximation for $\chi_{s,ij}(t,\xi_i)$ is given by:

$$\widetilde{\chi}_{s,ij}(t,\xi_i)=\xi_i\int_{ts}^{t}\dot{\chi}^s_j(T(t'))dt' \tag{24}$$

where it is assumed that secondary crystallization can be taken into account by an average value that evolves as a function of the thermal history. This is exactly what one measures when secondary crystallization is determined in a representative volume, i.e. when performing DSC or X-ray experiments. In this work we will use both assumptions, i.e. Equation (22) and Equation (24).

Finally, the overall multiphase crystallinity as a function of time is given by the sum of the primary and secondary crystallization processes.

$$\chi(t)=\chi_p(t)+\chi_s(t) \tag{25}$$

In the next section we will focus on how to determine the parameters for the secondary crystallization modelling.

### 3.3. The determination of $\chi^s_\infty$

To solve Equation (22), the evolution of the maximum level of secondary crystallinity is crucial. In the work of Yaghini and Peters [59], in which a polyamide 6 was studied, a kinetic maximum crystallinity level as a function of the temperature was reported. For entropy arguments a melt crystallized polymer will never reach 100% crystallinity, explaining the presence of this maximum $\chi^{KIN}_\infty$, which increases with increasing crystallization temperatures. This can be understood best by the fact that at high temperatures the material is allowed more time to crystallize, and therefore, solidifies in a state closer to the energetically most favorable state. A recent study of Auriemma et al. was devoted to reveal the crystallization behavior of blends of regular and irregular isotactic polypropylene fractions [56] with clearly separated crystallization temperature ranges. At high temperatures, progressive formation of lamellar crystals from the high stereoregular component was found. Consequently, the concentrations of the low stereoregular component in the remaining amorphous domains increased, and upon a further decrease in temperature, the low stereoregular component crystallized in thin lamellae in between the already existing primary ones. Although the different fractions in random PP are less obvious and less separated, it is plausible to assume that such a mechanism of phase separation as a result of crystallization takes place also here. Isothermal crystallization at high temperatures, i.e. low undercooling, gives rise to the formation of relatively thick lamellae [64,75]. Depending on the comonomer content distribution of the random PP, certain fractions of the material are not able to crystallize. Therefore, open spherulite structures with thick lamellae and relatively large amorphous layers in between, arise at high temperature where undercooling is low. However, upon subsequent cooling (after reaching full space filling), the undercooling gets larger, thinner lamellae can form, and additional parts of the amorphous material are able to crystallize. This suggests that when going from high to low temperature, the fraction of crystallizable material increases from zero towards higher levels, and is referred to as maximum crystallizable fraction $\chi^{CF}_\infty$ in this work. Ziegler-Natta materials generally contain non-crystallizable fractions, so the maximum (or plateau) value will not reach one.

From Alamo et al. [60], a maximum crystallinity is expected as a function of the isothermal crystallization temperature, when crystallizing PP with a high defect content in isothermal conditions. The decrease in crystallinity with increasing temperatures is attributed to a growing fraction of short sequences, present in the material, that can not participate in the crystallization process. This maximum shifts towards lower temperature with increasing defect content, and is (mainly) the result of primary crystallization phenomena. Considering the aforementioned local kinetic maximum crystallinity $\chi^{KIN}_\infty$ in combination with the local crystallizable fraction $\chi^{CF}_\infty$, it is assumed that the local maximum primary crystallinity, i.e. the maximum primary crystallinity in the filled space $\chi^p_\infty$, is given by their product.

$$\chi^p_\infty=\chi^{KIN}_\infty\cdot\chi^{CF}_\infty \tag{26}$$

Summarizing this information in a graph leads to the curves depicted in Fig. 1.

After reaching spacefilling, with a temperature dependent maximum primary crystallinity level $\chi^p_\infty$, explained by the product between $\chi^{KIN}_\infty$ and $\chi^{CF}_\infty$, the situation changes when proceeding to a different temperature. Upon lowering the temperature, the crystallizable fraction increases with respect to the temperature at which the primary crystals were formed initially. The $\Delta\chi^{CF}_\infty$ that comes available will form crystals at a crystallinity level of $\chi^{KIN}_\infty$, giving rise to a maximum increase in crystallinity, i.e. secondary crystallinity, of $\Delta\chi^{CF}_\infty\cdot\chi^{KIN}_\infty$.

$$\chi^s_\infty\left(T,\xi_{tp}\right)=\int_{\chi^{CF}_\infty\left(T_{t_p}\right)}^{\chi^{CF}_\infty(T)}\chi^{KIN}_\infty\left(T,\xi_{t_p}\right)d\chi^{CF}_\infty=\int_{T_{t_p}}^{T_t}\chi^{KIN}_\infty\left(T,\xi_{t_p}\right)\frac{d\chi^{CF}_\infty}{dT}dT \tag{27}$$

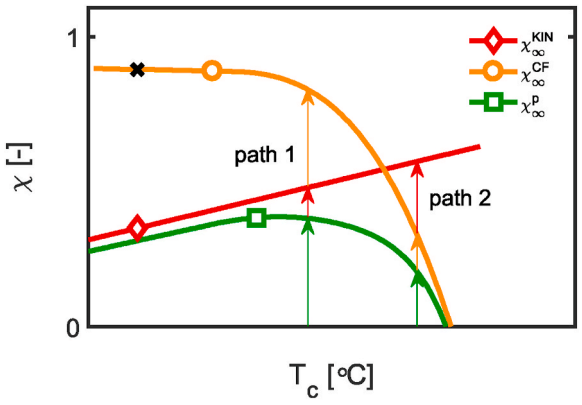


**Fig. 1.** Final crystallinity levels as a function of temperature for isothermal primary crystallization (green line), based on the amount of crystallizable material fraction (orange line) multiplied with the kinetic maximum crystallinity (red line). Arrows indicate the values of the aforementioned maxima, corresponding to 90°*C* and 125°*C*, indicated with 1 and 2 respectively (referred to as path 1 and path 2). (For interpretation of the references to color in this figure legend, the reader is referred to the Web version of this article.)

The maximum achievable amount of secondary crystallinity $\chi^s_\infty$ within the filled space $\xi$ is used in Equation (22), and follows from the integral over $\chi^{KIN}_\infty\left(T,\xi_{t_p}\right)$, Equation (27). $\xi_{t_p}$ in this equation accounts for the space filled at position $t_p$.

In Fig. 1, the positions of $\chi^{KIN}_\infty$ and $\chi^{CF}_\infty$ are captured by descriptive functions, in which the parameters have no physical meaning. $\chi^{CF}_\infty$ is captured by [76].

$$\chi^{CF}_\infty = C\frac{T_{m1}-T}{T_1-T} \tag{28}$$

while it is assumed that $\chi^{KIN}_\infty$ can be described by a first order polynomial, similar to Ref. [59]:

$$\chi^{KIN}_\infty = pk_1\cdot(T-273)+pk_2 \tag{29}$$

$pk_1$, $pk_2$, $C$, $T_{m1}$ and $T_1$ are constants, and $T$ is the temperature at which the crystalization takes place. For $T > T_{m1}$, $\chi^{CF}_\infty = 0$. The chosen strategy to determine $\chi^s_\infty$ (see Equation (22)) as a function of the thermal history will be explained on the basis of three hypothetical examples. We consider the $\chi^{CF}_\infty$ and $\chi^{KIN}_\infty$ values, as given in Table 1:

The values above result in the following calculations:

1. In the first case, isothermal crystallization till full space filling at low temperature (approximately 90°*C*) is considered, see Fig. 1 path 1. In this specific hypothetic case, the isothermal crystallization temperature is reached before the crystallization onset. $\chi^{KIN}_\infty = 0.5$ with a crystallizable fraction $\chi^{CF}_\infty = 0.8$, resulting in a $\chi^p_\infty = 0.5\cdot 0.8 = 0.4$, see Equation (26). At isothermal condition, $d\chi^{CF}_\infty/dT = \left[\chi^{CF}_\infty(T_t) - \chi^{CF}_\infty(T_{t_p})\right] = 0$, and thus secondary crystalization will not be possible (Equation (27)). However, after subsequent cooling to room temperature, the crystallizable fraction $\chi^{CF}_\infty$ has increased to 0.9, as indicated by the black cross in Fig. 1. Therefore, the term $d\chi^{CF}_\infty/dT = \left[\chi^{CF}_\infty(T_t) - \chi^{CF}_\infty(T_{t_p})\right] = 0.9-0.8 = 0.1$.

**Table 1**
Final crystallinity levels for illustrative calculation examples.

| Temperature [°*C*] | $\chi^{KIN}_\infty$ [ − ] | $\chi^{CF}_\infty$ [ − ] |
|---|---|---|
| 20 | 0.3 | 0.9 |
| 90 | 0.5 | 0.8 |
| 125 | 0.6 | 0.3 |

The kinetic maximum $\chi^{KIN}_\infty$ at that temperature is approximately 0.3. Then, according to Equation (27), $\chi^s_\infty = 0.3\cdot 0.1 = 0.03$. Notice that at full spacefilling, which was reached in the isothermal step of the hypothetical example, the local crystallinity values (within the filled space) equal the global crystallinity values (within entire sample) and thus, $\chi^{CF}_\infty = \chi_{\infty,CF}$,$\chi^{KIN}_\infty = \chi_{\infty,KIN}$ and $\chi^p_\infty = \chi_{\infty,p}$.

At a temperature of 90°*C*, the $\chi^{CF}_\infty$ is close to reaching the lower temperature plateau value, meaning that further cooling hardly affects the crystallizable fraction. Consequently, with primary crystallization at increased undercooling, the population of secondary lamellae (cross-hatched structures) decreases [77].

2. In case isothermal crystallization (till full spacefilling) at high temperature is considered, for example 125 *C* as indicated in Fig. 1; path 2, the proportions of primary and secondary crystallization change with respect to the first example. $\chi^{KIN}_\infty = 0.6$ with a crystallizable fraction of $\chi^{CF}_\infty = 0.3$, resulting in a $\chi^p_\infty = 0.6\cdot 0.3 = 0.18$ (Equation (26)). Also in this case, at isothermal conditions $\chi^s_\infty = 0$ (Equation (27)). After subsequent cooling to room temperature, $d\chi^{CF}_\infty/dT = \left[\chi^{CF}_\infty(T_{current}) - \chi^{CF}_\infty(T_{formed})\right] = 0.9-0.3 = 0.6$, and $\chi^{KIN}_\infty = 0.3$. Then, $\chi^s_\infty = 0.3\cdot 0.6 = 0.18$ as obtained by Equation (27). The fraction of secondary crystals that can be formed when following path 2 is thus an order of magnitude higher than the fraction of secondary crystals formed in case 1.
3. Finally, a situation with an additional quenching step at 50% spacefilling is considered. The first isothermal crystallization, up to 50% spacefilling ($\Delta\xi_1$), occurs at high temperature; 125 °*C*. The second subsequent isothermal crystallization step, from 50% spacefilling till 100% ($\Delta\xi_2$) takes place at 90°*C* (combination of path 1 and 2, Fig. 1). With $\chi_{\infty,KIN} = 0.6$ and 0.5, and $\chi^{CF}_\infty = 0.3$ and 0.8 respectively, this results in a global primary crystallinity

$\chi_{\infty,p} = \Delta\xi_1\cdot\chi^p_{\infty,@125} + \Delta\xi_2\cdot\chi^p_{\infty,@90} = \Delta\xi_1\cdot\chi^{KIN}_{\infty,@125}\cdot\chi^{CF}_{\infty,@125} + \Delta\xi_2\cdot\chi^{KIN}_{\infty,@90}\cdot\chi^{CF}_{\infty,@90} = 0.5\cdot 0.6\cdot 0.3 + 0.5\cdot 0.5\cdot 0.8 = 0.29$.

After quenching to a temperature of 20°*C*, the crystallizable fraction $\chi^{CF}_\infty = 0.9$, and thus

$\chi_{\infty,s} = \Delta\xi_1\cdot\chi^s_{\infty,1} + \Delta\xi_2\cdot\chi^s_{\infty,2} = \Delta\xi_1\cdot\chi^{KIN}_{\infty,@20}\cdot(\chi^{CF}_{\infty,@20} - \chi^{CF}_{\infty,@125}) + \Delta\xi_2\cdot\chi_{\infty,@20}{}^{KIN}\cdot(\chi^{CF}_{\infty,@20} - \chi^{CF}_{\infty,@90}) = 0.5\cdot 0.3\cdot(0.9-0.3) + 0.5\cdot 0.3\cdot(0.9-0.8) = 0.115$. Please note the distinction between local and global crystallinities in this last example.

Using the model as explained in these examples means that phase separation during crystallization is implicitly taken into account. Crystallization is resulting from the fractions containing sufficiently long propylene sequence lengths. Depending on the temperature, parts of these fractions participate in crystallization, or are forced into the remaining amorphous domains. In real life processing, crystallization will not proceed in a stepwise fashion, but solving the integrals allows to apply the same procedure on more realistic conditions. Although difficult to visualize, the scenario's shown before clarify how the model works. Moreover, one could reason why secondary crystallization plays a major role in the crystallization behavior of PP random copolymers, while in highly isotactic PP homopolymer no such phenoma are observed (at least to this extend). Due to longer average sequence lengths in the major part of a homopolymer, the plateau of the temperature dependent crystallizable fraction is observed at higher temperatures. Therefore, in the temperature range where the homopolymers typically crystallize, the maximum crystallinity is dominated by $\chi^{KIN}_\infty$.

## 4. Materials and methods

### 4.1. Material

The material used in this work is an ethylene propylene random copolymer, supplied by SABIC$^{TM}$. The ethylene content, determined by $^{13}$C NMR is approximately 3.7 wt%. The material is synthesized with a

Ziegler-Natta catalyst, and has a weight average molecular mass Mw of 690 kg/mol, with a polydispersity index Mw/Mn of approximately 7.7 (SEC-DV-IR). The MFR of the material is 0.3 $g/10$ min at 230°$C$.

### 4.2. Polarized optical microscopy

The primary growth rate of the crystallizing morphology is quantified by means of polarized optical microscopy (POM). Thin polymer films (≈50–100 μm) are prepared by heating single granules to 230 °$C$ on a hot plate. These molten droplets are then manually compressed between two microscope glass slides and left at high temperature for 2 min to relax any stresses introduced during the compression step. The films are sandwiched between a microscope glass slide and cover glass slide and placed in a Linkam LTS350 hotstage. For each crystallization protocol a series of images is acquired in transmission mode using an Olympus BX51 microscope equipped with an LM-PLAN-FI 20x/040 lens. To enhance the contrast between the crystalline lamellae and amorphous undercooled melt, the hotstage is placed between two orthogonal polarizers. The sample is heated to 230 °C to erase the thermo-mechanical history and subsequently cooled at a rate of 30 K/min to the desired temperature. Due to the limited achievable cooling rates, only a relatively small crystallization temperature window can be assessed in the optical microscopy experiments. After reaching the set temperature, the sample is kept isothermal while collecting an image series to follow the spherulite growth over the complete crystallization process till impingement. The linear growth rate $G(T)$ is obtained from the slope of average plots of the spherulite radius versus the time. With pixel size of 17 μm × 17 μm, and an image of 2576 x 1932 pixels, several radii were recorded per crystallization temperature to reduce the experimental uncertainties. When setting a threshold gray value to define the space filled area, the conversion of the polymer melt into solidified material can be determined over time.

### 4.3. Fractionation

The PPR is fractionated by means of preparative Temperature Rise Elution Fractionation (pTREF). A cooling rate of 0.025 °C/min is used in the cooling process on a sample of 2 g. At every fractionation temperature, i.e. 20, 55, 75, 84, 89, 92, 95, 98 and 110 °$C$, after annealing for 1 h xylene solvent is flushed 3 times to recover the soluble material. Subsequently, methanol is used for precipitation, and after drying, the sample is suitable for further analysis.

### 4.4. NMR

The ethylene content of the copolymers is determined by $^{13}$C NMR spectroscopy. Approximately 150 mg of each sample is dissolved at 135 °$C$ in ~3 ml of 1,1,2,2-tetrachloroethane-d2 (TCE-d2) in a 10 mm NMR tube. The NMR measurements are carried out on a Bruker 500 Advance III HD spectrometer equipped with a 10 mm DUAL (proton and carbon) cryogenically cooled probe head operating at 125 °$C$. The $^{13}$C NMR experiments are performed using power-gated decoupling, a spectral width of 220 ppm and a relaxation delay of 20 s between each of the 512 transients. The spectra are calibrated by setting the central signal of TCE's triplet at 74.2 ppm.

### 4.5. Thermal analysis

In order to quantify the crystallization behavior, two different temperature protocols are used; isothermal crystallization and crystallization during continuous cooling. To measure the crystallization rate and the corresponding half time, isothermal DSC experiments were conducted on a TAinstruments Q20. The maximum specified cooling rate in this DSC apparatus is 30 °C/min, and therefore, the accessible temperature range for achieving purely isothermal crystallization is rather limited. To study crystallization behavior at high undercooling, a differential fast scanning chip calorimeter FLASH DSC 1 (Mettler Toledo), combined with a Huber Intracooler TC100, is used [55,61]. The detailed procedure and the applied thermal protocols are explained in detail in the Supplementary Material.

### 4.6. X-ray

To capture the structure development of the PPR under various conditions, a series of X-ray experiments are carried out. These experiments consist of two series of in-situ measurements, and are completed with ex-situ experiments, of which the details are discussed separately. The data analyses of the integrated X-ray patterns is described in the Supplementary Material.

#### 4.6.1. Isothermal crystallization with in-situ X-ray

The crystallization behavior is studied with a Linkam DSC600 hot stage, equipped with a liquid nitrogen container for fast cooling. This stage allows for cooling in a controlled way up to rates of 30 °C/min and to record the enthalpy from the crystallization process. The applied temperature history is depicted in Fig. 16a, following the solid line (cooling after the isothermal step). These experiments are combined with in-situ real time WAXD experiments, carried out at the ESRF DUBBLE BM26, Grenoble, France. The evolution of the fractional content of the different polymorphs could be observed by deconvolution of the integrated signal [5]. The WAXD experiments are also combined with real time simultaneous SAXS experiments to capture the evolution of the long period [78]. The 2D SAXS patterns are recorded with a Pilatus 1 M detector, and simultaneously a Pilatus 3K detector is used to record the WAXD signals. Both the detectors have a pixel size of 172 × 172 $\mu m^2$, and the sample to detector distance was approximately 290 mm for WAXD and 3000 mm for SAXS. The acquisition time was 5 s for both SAXS and WAXD. The wavelength of the beam is $\lambda = 1.033\mathring{A}$. All samples are background subtracted and normalized to incident beam intensity, prior to the radial integration, which is executed using the Fit2D software.

#### 4.6.2. Continuous cooling experiments with in-situ X-ray

In a second set of experiments at the Twente University, continuous cooling is carried out on a custom installed Linkam THMS600 hot-stage, combined with in-situ WAXD experiments performed in transmission mode and conducted on a Bruker D8 Discover system. The XRD system is equipped with a Cu-source, providing a wavelength of 1.54 $\mathring{A}$. A Montel optical mirror is used to provide a highly parallel beam, collimated to a diameter of 1 mm. The sample in the hot-stage was enveloped in Kapton which was installed at 68 mm from the Eiger R500K 2D detector. Constant cooling conditions of 20, 5 and 1 °C/min are applied, and measured with acquisition times of 9, 36 and 58 s per frame respectively, resulting in average temperature resolutions of 3, 3 and 1 °$C$ per frame. Samples are heated and cooled according to the protocol indicated in Fig. 16b. An interval of 2 s was required in between measurement frames to store the data. Background subtraction and integration is executed using the Fit2D software. The experiment at the highest cooling rate, i.e. 20 °C/min is executed 4 times, and the recorded patterns were summed to improve resolution.

#### 4.6.3. Ex-situ X-ray

Additionally, single shot experiments were conducted on DSC samples prepared with different cooling rates. Static experiments on these preconditioned samples were performed at the SAXSLAB GANESHA at DSM Material Science Geleen. The instrument features a XENOCS microfocus source ($CuK_\alpha$) coupled to a multilayer optics. Depending on experimental conditions, the primary beam is shaped via three sets of JJXRAX 4-blade slit systems with single-crystal antiscatter slits to increase signal-to-noise ratio. Samples are mounted in vacuum and

positioned via a remote-controlled stage, with a Pilatus 300k detector placed at a distance of 120 mm from the sample position in an off-axis position to extend the available q-range during WAXD experiments. Raw data are calibrated and intensity profiles extracted after standard corrections from the non-oriented samples via sectorial integration using the SAXSLAB software.

Finally, two samples prepared in the Flash DSC at isothermal crystallization temperatures of 60 and 90 $^{\circ}C$ were measured ex-situ to reveal the phase composition. The latter two samples were cooled with 1000 °C/s after isothermal crystallization, to ensure that the structures created at the isothermal temperatures were frozen, and secondary crystallization phenomena were minimized. These static experiments on samples prepared via Flash-DSC where performed using the D8 DISCOVER at DSM Material Science Geleen. The instrument features an INCOATEC microfocus source ($CuK_{\alpha}$) with a multilayer optics focusing the beam onto the sample position. WAXD patterns are collected using a VANTEC 500 detector placed at a distance of 150 mm from the sample, a take-off angle of $2\Theta = 18^{\circ}$ using a reduced resolution of 1024 x 1024 pixels. To match dimensions of the primary beam and FDSC sample, the beam was reduced to size of either 20 or 50 μm using capillary optics with a lead pinhole mounted near the sample to reduce air scatter. Prior to measurements the sample position was optimized by monitoring diffracted intensity while moving y- and z-position of the remote-controlled sample stage.

## 5. Results and discussion

### 5.1. Parameterization strategy

As became evident in Section 3, the model framework contains a significant number of parameters, which partially results from the distinction between primary and secondary crystallization phenomena (needed to describe and model the in-situ experiments), and partially as a consequence of the polymorphism due to co-crystallization of $\alpha$ and $\gamma$ structures, typically observed for PPR's. For this reason, an approach based on solely DSC as for example proposed by de Santis et al. [79], is not applicable. Therefore, the first part of the method to parametrize the model is based on a stepwise procedure, consisting of the following experiments to capture the primary crystallization kinetics:

- Optical microscopy experiments, carried out at high temperature in the range where isothermal crystallization can be achieved, are analyzed first. From these experiments, the heterogeneous nucleation density and the spherulitic $\alpha$ growth rate for this limited temperature range can be extracted.
- A combination of crystallization half times in the heterogeneous crystallization regime, obtained from DSC, Flash DSC and optical microscopy, is then used to fix the position and shape of the spheruletic $\alpha$ growth rate as well as the heterogeneous nucleation density, both as a function of the crystallization temperature.
- With the $\alpha$ growth rate fixed, experimental information on phase composition obtained from X-ray is utilized to determine the ratio of $\alpha$ versus $\gamma$ crystals. In this way, the position and shape of the $\gamma$ growth rate (modeled as an apparent growth rate, see Equations (3) and (8)) can be found and fixed.
- Finally, the position of the homogeneous nucleation (mesophase) density and corresponding growth rate is optimized by means of numerical exprimenting, based on a combination of reasoning and experiments conducted with Flash DSC.

Once the primary crystallization kinetics are captured, the temperature dependent final crystallinity levels and the secondary crystallization kinetics are determined on the basis of X-ray and DSC:

- The equilibrium level of crystallinity upon primary crystallization, $\chi_{\infty}^{p}$, is determined based on a combination of WAXD, DSC and Flash DSC experiments, all covering a specific temperature range.
- The temperature dependent crystallizable fraction, $\chi_{\infty}^{CF}$, is determined via NMR on fractionated PPR. Combining the average propylene sequence length determined as such, with the lamellar thickness as a function of the crystallization temperature, results in the crystallizable fraction as a function of the crystallization temperature.
- By dividing $\chi_{\infty}^{p}$ by $\chi_{\infty}^{CF}$, the kinetic maximum crystallinity $\chi_{\infty}^{KIN}$ can be obtained. Here it is asumed that $\chi_{\infty}^{KIN}$ can be described by a first order polynomial [59].
- Ultimately, in-situ X-ray (WAXD and SAXS) is used to optimize the parameters describing the secondary kinetics for both the $\alpha$ and $\gamma$ growth.

After presenting the parametrization results, the model is applied to a series of different isothermal crystallization and continuous cooling experiments. Once the validity of the approach has been demonstrated, structure development is predicted over a wide range of processing relevant cooling conditions.

### 5.2. Optical microscopy

The isothermal optical microscopy experiments are conducted in a range between 114 $^{\circ}C$ and 126 $^{\circ}C$, with intervals of 2 $^{\circ}C$. At lower temperatures, the desired temperature could not be reached prior to the crystallization onset, while at higher temperatures the required experimental time to reach spacefilling was too long. In Figure 18, Supplementary Material, POM images are shown at different times, corresponding to crystallization temperatures of 114, 120 and 126$^{\circ}C$.

At early stages, elongated spherulites which are typical for crystallization of $\alpha$ phase skeletons with $\gamma$-phase cross hatching, are encountered [80]. In later stages, the growth proceeds in a more spherical fashion. As expected, the highest amount of spherulites is obtained at the lowest crystallization temperature, and therefore, giving the smallest spherulites. Counting the amount of spherulites visualized in the POM image is a delicate task, but can be used to determine the nucleation density according to:

$$N(T) = N_{2D}^{(3/2)} \tag{30}$$

Here, $N_{2D}^{(3/2)}$ is the amount of nuclei that are observed in the 2D image [54,81,82]. The equation only applies if the image is sufficiently large with respect to the spherulites. An example of the counting, as well as the temperature dependent nucleation density is shown in Figure 19a and 2a respectively. The solid line follows from Equation (10), using the parameter values as listed in Table 2, and is in qualitative agreement with nucleation densities reported previously by various authors [6,7,54,83–85].

In quiescent conditions at temperatures above the melting range of the mesophase, the formation of the $\alpha$ skeleton governs spacefilling and dominates the spherulite growth, whereas the formation of $\gamma$ proceeds via branching on the $\alpha$-lamellae [18,22,80]. Therefore, it is assumed that determination of the radius as a function of time allows for a direct measurement of the $\alpha$ growth rate. This is done for all optical microscopy experiments and the results are shown in Fig. 19b. At every temperature, several spherulites are tracked in order to reduce the statistical error. The values of the different slopes fitted to the radius over time reveal the growth rates. Note that the extrapolated slopes do not intersect with the origin, as was previously reported by for example [22,105]. The growth rates are plotted in Fig. 2b as a function of the crystallization temperature. In addition to the data obtained in this work, an extensive comparison is made with data reported in literature, containing both iPP homopolymers and PPR's. Based on the data reported in Refs. [4,22] (PPR), and in Refs. [86–88] (iPP homopolymers with

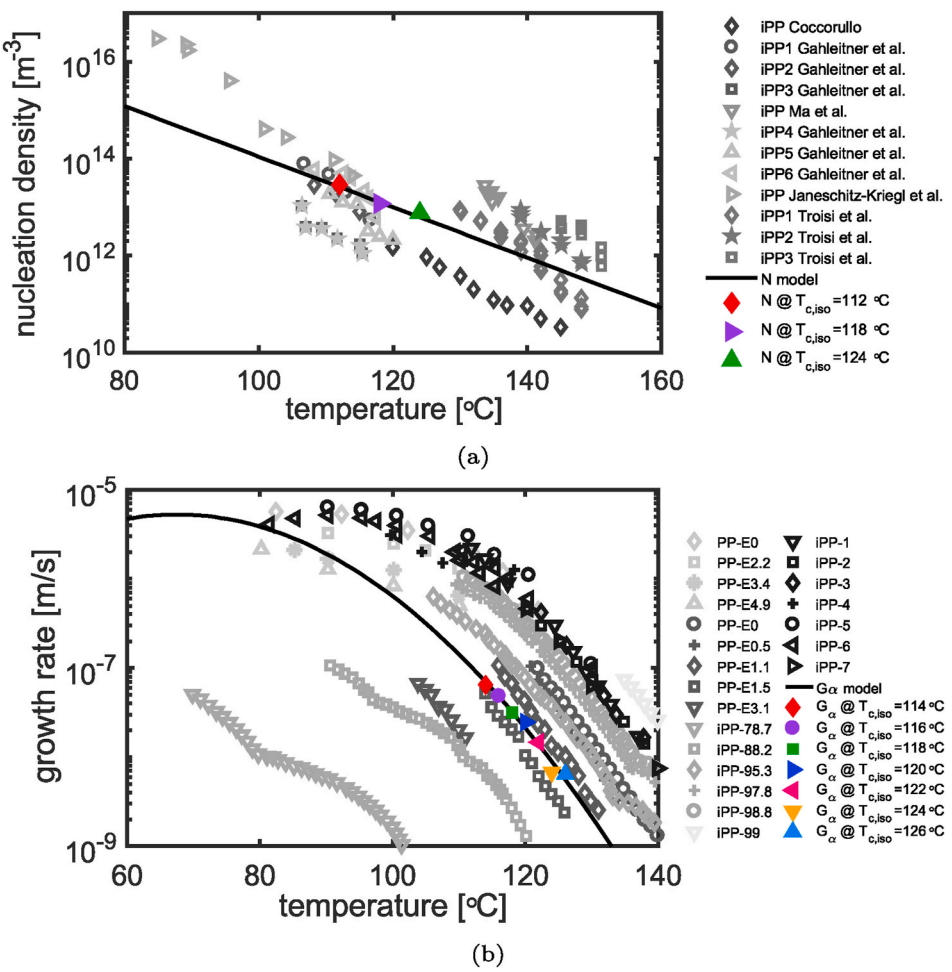


**Fig. 2.** a) The heterogeneous ($\alpha$ crystal) nucleation density as a function of the temperature. The iPP data is obtained from Refs. [6,7,54, 83–85] respectively, and the colored markers are obtained from POM experiments carried out in this work. The line represents the extrapolation used in the model. b) PP-E data is obtained from Ref. [4] (ZN catalyst) and [22] (metallocene catalyst). The number indicates the weigth percentage of ethylene. The iPP data is reproduced from Ref. [86] (fractionated iPP) and [87] (metallocene catalyst), where the number indicates the isotacticity. Finally, iPP-1 to iPP-7 are a series of highly isotactic iPP's, reproduced from Ref. [88]. The colored markers are the growth rates measured in this study.

**Table 2**
Model parameters.

| Parameter | Value | Unit | Parameter | Value | Unit |
|---|---|---|---|---|---|
| $N_{ref}$ | $10^{13}$ | [#] | $G_{max,m}$ | $6.5 \cdot 10^{-6}$ | [$m/s$] |
| $T_{Nref}$ | 393 | [$K$] | $T_{G,ref,m}$ | 298 | [$K$] |
| $c_n$ | 0.12 | [$1/K$] | $c_{g,m}$ | $1.2 \cdot 10^{-3}$ | [$1/K^2$] |
| $G_{max,\alpha}$ | $5.27 \cdot 10^{-6}$ | [$m/s$] | $N_{max,h}$ | $3.05 \cdot 10^{18}$ | [$\#/m^3$] |
| $T_{G,ref,\alpha}$ | 340.5 | [$K$] | $c_{n,h}$ | $2.1 \cdot 10^{-3}$ | [$1/K$] |
| $c_{g,\alpha}$ | $8 \cdot 10^{-3}$ | [$1/K^2$] | $T_{Nref,h}$ | 292.02 | [$K$] |
| $G_{max,\gamma}$ | $1.82 \cdot 10 - 6$ | [$m/s$] | | | |
| $T_{G,ref,\gamma}$ | 344.45 | [$K$] | | | |
| $c_{g,\gamma}$ | $1.85 \cdot 10^{-3}$ | [$1/K^2$] | | | |

different levels of isotacticity), it can be seen that the maximum of the growth rate decreases in absolute value, but also shifts towards lower temperatures with an increasing amount of defects. From this comparison it is clear that the ethylene content is not the only factor of influence. The Ziegler-Natta PPR used in this work (ethylene content = 3.7 wt %) displays a growth rate in between metallocene based PPR's with a ethylene content of 1.1 and 1.5 *wt%* respectively. In fact, Kang et al. correlated the temperature dependent growth rate to the longest sequence lengths present in the polypropylene [89,90]. This illustrates the importance of the chemical composition distribution of the material. The data obtained from the combination of the POM experiments and the literature allows to position the $\alpha$-growth rate and nucleation density.

### 5.3. Isothermal crystallization with in-situ X-ray

Now, $N_\alpha(T)$ and $G_\alpha(T)$ are fixed (parameter values in Table 2). In order to continue the parameterization of the primary crystallization model, the $G_\gamma(T)$ has to be determined and for that purpose, (in-situ) X-ray experiments are used. Due to the co-crystallization of $\gamma$-lamellae into $\alpha$ spherulites, $\gamma$-growth rate cannot be visualized by means of a direct optical measurement. Therefore, the apparent growth rate is deduced from an optimization of the model on experimental X-ray data, captured during primary isothermal crystallization. The different experimental techniques employed in this work are calibrated for the temperature on the basis of the crystallization half times, according to the method described in the Supplementary Material.

During the isothermal crystallization, both the $\alpha$- and $\gamma$-polymorphs are formed. From the peak deconvolution procedure it follows that the ratio of $\alpha$ and $\gamma$ is approximately constant throughout the primary crystallization process, at a ratio depending on the isothermal crystallization temperature, see Fig. 3. Based on the definition of the primary crystalization, this behavior is expected. At the front of growing spherulites, the amorphous PPR consists of a homogeneous melt that gives rise to a fixed ratio of $\alpha$ and $\gamma$ crystals. Moreover, lamellar thickening and perfectioning is neglected, and other secondary phenomena like lamellar insertion due to growing crystallizable fractions does not take place at isothermal conditions. At these conditions and with one single nucleation density, the ratio in the volume fraction $\gamma$ versus $\alpha$ scales with $G_\gamma^3/(G_\alpha^3 + G_\gamma^3)$. This is used to position the $\gamma$ growth rate with respect to the $\alpha$ growth rate. Since the available crystallization temperature range in the DSC is relatively small, similar types of experiment was carried

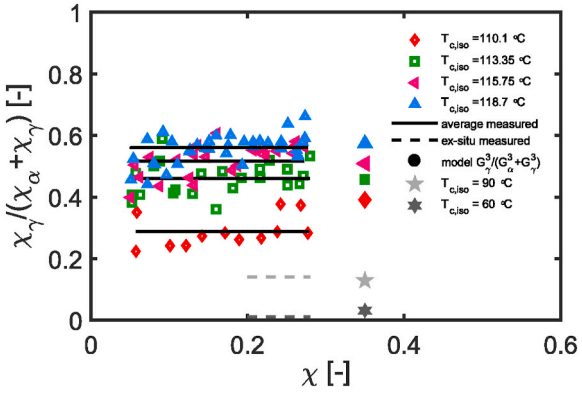


**Fig. 3.** The $\gamma$ fraction as a function of the crystallinity during primary crystallization (open markers) under isothermal conditions. The solid black lines represent the average constant $\gamma$ crystallinity throughout the crystallization process. Dashed lines indicate $\gamma$ crystallinity as obtained from ex-situ experiments, carried out on flash DSC chips isothermally crystallized at 60 and 90 °C. The filled markers are obtained from the ratio's in cubic growth rate of $\alpha$- and $\gamma$ phase, as calculated by the model.

out in the Flash DSC at an isothermal crystallization temperatures of 60 °C and 90 °C. The preconditioned samples are quenched to room temperature and used to conduct ex-situ WAXD experiments (see Figure 21, Supplementary Material). Crystalline fraction of $\gamma$ = 0.01 and 0.14 respectively). The broader temperature range and the additional data obtained via Flash DSC help to position the $\gamma$ growth rate over a broad temperature regime. Consequently, the applicability is extended to a wider range of cooling rates. By using the combined information, the growth rate curve of the $\gamma$-crystals can be fixed, see Fig. 4b. The X-ray is used to manually optimize for the ratio between $\alpha$ and $\gamma$. In Section 5.5, a more extensive analysis of the X-ray results is presented.

The last that needs to be parametrized in the primary part of the crystallization model concerns the mesophase, which forms via a homogeneous nucleation mechanism. Crystallization in the relevant temperature regime can only be assessed in a controlled way by using the Flash DSC. The crystallization half times, determined over a broad range of isothermal crystallization temperatures, see Figure 20b, allow to estimate the parameters of the governing equations. The choice to describe the homogeneous nucleation rate by Equation (11) simplifies the parameterization process. Nevertheless, a basic principle needs to be considered. The nodular structure of the mesophase, which is typically finer than the spheruletic morphologies, implies a relatively high nucleation density, i.e., the homogeneous nucleation rate will exceed the heterogeneous nucleation rate in the temperature regime in which it is active (in between the melting temperature of the mesophase and the glass transition temperature of the melt which typically varies with ethylene content [91]). Based on these considerations, the homogeneous nucleation rate is described with the parameters reported in Table 2, and depicted in Fig. 4a. Fixing the mesophase nucleation density allows to fit the corresponding growth rate on the crystallization half times, measured in the low isothermal crystallization temperature range. The result of this exercise is depicted in Fig. 4b. The combination of nucleation- and growth rate is not uniquely determined for the mesophase, however, captures the experiments sufficiently well.

### 5.4. The determination of the $\chi_\infty$ levels

To include secondary crystallization in the model, and to be able to predict also the final level of the crystallinity on the basis of the conditions experienced by the material, the temperature dependent maximum crystallinity levels need to be determined. The final level of the primary crystallinity $\chi_\infty^p$ can be measured directly in isothermal conditions and the crystallizable fraction $\chi_\infty^{CF}$ can be deduced from experiments as well. According to Equation (26), $\chi_\infty^{KIN}$ then needs to be determined by dividing $\chi_\infty^p$ by the crystallizable fraction, since particularly $\chi_\infty^{KIN}$ is difficult to measure. The crystallizable fraction is referring to the fraction of chains with a sufficiently long sequence of propylene units to crystallize into lamellae at a given undercooling. At decreasing crystallization temperature, the lamellar thickness decreases, meaning that the crystallizable fraction increases. To get this material characteristic as a function of temperature, different paths may be chosen. Here, a route via fractionation and $^{13}$C NMR will be discussed, which is the most comprehensive approach.

The PPR used in this study is fractionated into nine separate fractions. The corresponding results are summarized in Table 3. The composition and sequence length distribution are determined for every fraction. The composition on the triad level, as determined via NMR can be used to calculate the average regular sequence length [92,93], $iPP_{avg}$ of each fraction, according to Equation (31).

**Table 3**
NMR results on fractionated PPR.

| fraction # | relative amount | *PPP* [%] | *PPE* [%] | *EPE* [%] | $iPP_{avg}$[#] | $iPP_{avg,l}$[*nm*] | *C2* [*wt %*] |
|---|---|---|---|---|---|---|---|
| 1 | 5.8 | 42.2 | 22.3 | 7.5 | 5 | 1.1 | 20.3 |
| 2 | 6.4 | 72.7 | 14.9 | 1.6 | 11 | 2.4 | 7.1 |
| 3 | 9.3 | 83.9 | 9.8 | 0.5 | 18 | 3.9 | 3.9 |
| 4 | 8.7 | 88.2 | 7.5 | 0.2 | 25 | 5.4 | 2.6 |
| 5 | 10.4 | 90.1 | 6.3 | 0.2 | 30 | 6.5 | 2.3 |
| 6 | 7.8 | 91.3 | 5.7 | 0.2 | 33 | 7.2 | 2.2 |
| 7 | 8.3 | 92.3 | 5.1 | 0.1 | 37 | 8.0 | 2.1 |
| 8 | 28.8 | 92.9 | 4.9 | 0.1 | 39 | 8.5 | 1.5 |
| 9 | 13.5 | 94.6 | 3.8 | 0.0 | 51 | 11.1 | 1.4 |

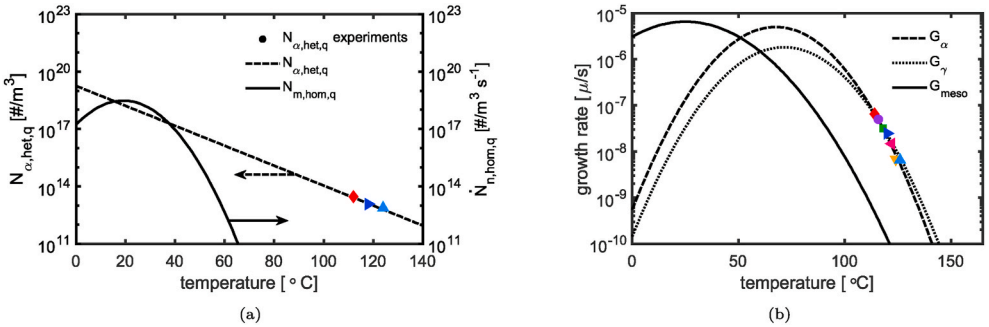


**Fig. 4.** a) The heterogeneous nucleation density (dashed line) and the homogeneous nucleation rate (solid line) as used in the model. The markers indicate the nucleation densities obtained from the POM experiments. b) Growth rates of $\alpha$ (dashed), $\gamma$ (dotted) and mesophase (solid) as used in the model. The markers indicate the alpha phase growth rates obtained from optical microscopy.

$$iPP_{avg} = \frac{2PPP + PPE}{PPE} \tag{31}$$

In this equation, *PPP* is the relative percentage of triads consisting of three propene monomers, and *PPE* the percentage of two propene units followed by one ethylene monomer.

When the material crystallizes, it first adopts a helical conformation with a repetitive length of 0.65 nm per 3 propene monomers. Therefore, the average iPP sequence length can be translated into a helical length in *nm*, according to equation (32).

$$iPP_{avg,l} = 0.65\left(\frac{iPP_{avg}}{3}\right) \tag{32}$$

The fraction containing the fewest ethylene comonomers, i.e. fraction nine, has an average propylene sequence length of 51 units, see Table 3. This fraction covers 13.5% of the material and can form lamellae with a thickness of approximately 11.1 nm according to equation (32). Fraction eight, which is 28.8% of the lamellae can form lengths of approximately 8.5 nm, meaning that in total 42.3% of the material can form lamellae of at least 8.5 nm. Repeating this for all ractions yields the result reported in Fig. 5a.

After interpolation of the results, one can look for example at an average iPP length $iPP_{avg,l}$ of 8 nm, and read that a material fraction of approximately only 45–50% can contribute to the crystallization process. This curve is a material characteristic which affects the crystallization behavior, because the temperature at which crystallization takes place determines the amount that can crystallize. It should be noted that the NMR analyses based on the fractions is a fingerprint of the catalyst and the process used for producing the specidic polymer investigated in this study, and does not apply to all PPR's [95]. The thickness of the lamellae that are being formed can be deduced from the melting temperature via Gibbs-Thomson [63–65]. By combining with the Hoffman-Weeks equation, lamellar thickness can also be predicted from the crystallization temperature [66]. In case the thickening factor of the Hoffman-Weeks relation is set to 1, $l_c$ and $T_c$ relate according to:

$$l_c = \frac{2\sigma_e T_m^0}{\Delta H_f\left(T_m^0 - T_c\right)} \tag{33}$$

Fig. 5b shows the dependence of the lamellar thickness on the crystallization temperature for an iPP, as well as a PPR with a comonomer content of 3.1 wt% ethylene [33]. At low isothermal crystallization temperatures, the lamellar thickness converges to an asymptotic value of approximately 2–3 nm, indicating a minimum lamellar thickness that can be formed [96], see asymptote in Fig. 5b. Besides the amount of ethylene, polymorphism can influence the Gibbs-Thomson equation [33]. The solid and the dashed lines represent the $\alpha$ and the $\gamma$ polymorphs respectively. The parameters for the Gibbs-Thomson equation applicable to the PPR used in this study are based on a fit of data obtained in isothermal crystallization experiments carried out with in-situ X-ray (lamellar thickness $l_c$), and a determination of $T_m^0$ based on DSC, see Figure 23. Note that $T_m^0$ values depend on the content of imperfections [97,98]. To avoid the complex interplay between melting, reorganization, recrystallization and decomposition [61], the sample is crystallized isothermally and heated with a rate of 10 °C/min, which is sufficiently high [40].

Although part of the ethylene can be included in the polypropylene crystals [21,32,62,99], the majority is excluded. Consequently, it is assumed that only the regular isotactic fractions long enough to be incorporated in lamellae (formed at a given temperature) will participate in the crystallization process. Folding back of chains into the crystal and the position of the ethylene units in that perspective has consequences too, but is not considered here. In that way, the results in Fig. 5 can be combined to obtain a crystallizable fraction $\chi_\infty^{CF}$ as a function of the crystallization temperature in a way similar to Jeon et al., who determined a fractional content of crystallizable sequences as a funtion of ethylene content [91]. In the current work the ethylene content of the material is constant and the crystalizable fraction is solely a function of temperature. The higher the crystallization temperature and the thicker the lamellae, the smaller the fraction of material that crystallizes, see Fig. 6, orange line. The values, used to parameterize the polynomial in Equation (28), are given in Table 5.

To use this approach on a ZN random copolymer, which has a broad distribution of comonomer (as illustrated by the fractionation experiment, Table 3), the fractions should not phase separate in the polymer melt prior to crystallization. In this stage, possible phase separation is determined by the miscibility of the different fractions present in the sample and the thermo-mechanical history the material experiences. For PP random copolymer, the fractions eluted at temperatures above 55°*C*

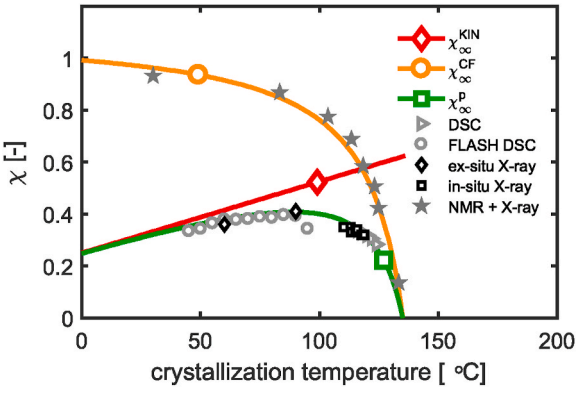


**Fig. 6.** The crystallizable fraction $\chi_\infty^{CF}$ (orange line) as a function of the crystallization temperature, based on NMR conducted on the PPR fractions (experimental data as a function of the crystallization temperature obtained from Equation (33) and Table 3).In green, the primary crystallinity level $\chi_\infty^{p}$, based on DSC- and X-ray experiments (markers), is shown. The final kinetic crystallinity level $\chi_\infty^{KIN}$ (red curve) as obtained from Equation (26). (For interpretation of the references to color in this figure legend, the reader is referred to the Web version of this article.)

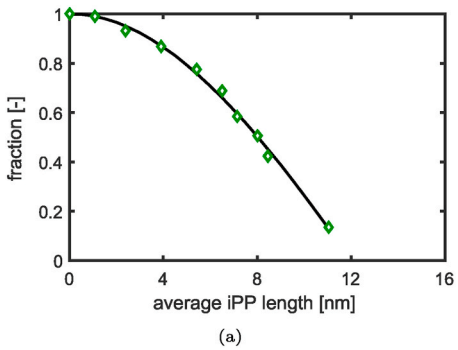


(a)

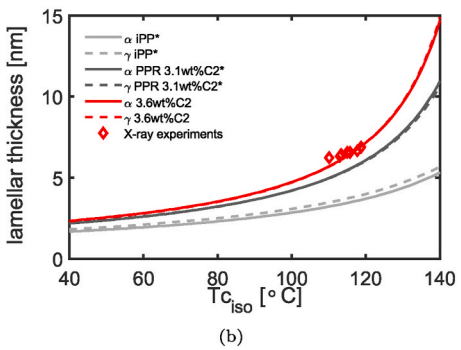


(b)

**Fig. 5.** a) The fraction of the PP random with a minimal isotactic propylene sequence length as indicated on the horizontal axis, in which the average iPP length is the length in the helical conformation. The curve is calculated based on fractions obtained via pTREF (fractionation based on melting behavior) and evaluated individually with NMR. b) Relation between lamellar thickness and crystallization temperature for a PP-hopol [94], a PPR [33], and the PPR used in this work. The parameters are given in Table 4.

**Table 4**
Parameters for the Gibbs-Thomson equation, Equation (33), for both the $\alpha$ and $\gamma$ phase.

| Parameter | iPP [94] | PPR [33] | PPR this study | Unit |
|---|---|---|---|---|
| ethylene content | 0 | 3.1 | 3.7 | [*wt%*] |
| $\sigma_{e,\alpha}$ | $52.2 \cdot 10^{-7}$ | $57 \cdot 10^{-7}$ | $61 \cdot 10^{-7}$ | $[J/cm^2]$ |
| $T^0_{m,\alpha}$ | 459.1 | 483 | 434.07 | $[K]$ |
| $\Delta H_{f,\alpha}$ | 209 | 199 | 191 | $[J/g]$ |
| $\sigma_{e,\gamma}$ | $51.7 \cdot 10^{-7}$ | $52 \cdot 10^{-7}$ | $52 \cdot 10^{-7}$ | $[J/cm^2]$ |
| $T^0_{m,\gamma}$ | 460.2 | 439 | 431.5 | $[K]$ |
| $\Delta H_{f,\gamma}$ | 190 | 180 | 179 | $[J/g]$ |

**Table 5**
Model parameters for the $\chi_\infty$ levels.

| $\chi^{CF}_\infty$ | value | $\chi^{KIN}_\infty$ | value |
|---|---|---|---|
| $C$ | 1.11 [-] | $pk_1$ | $2.75 \cdot 10^{-3}$ [-] |
| $T_{m1}$ | 408 [K] | $pk_2$ | $2.5 \cdot 10^{-1}$ [-] |
| $T_1$ | 421 [K] | | |

may be expected to be miscible in the melt. All these fractions contain 1.4–3.9 *wt%* ethylene, so they differ in branching content by less than 4 *mol%*. Hence, miscibility between these fractions is expected. For the material analyzed, the fractions potentially sensitive to phase separation during high temperature annealing ($>10$*wt%* ethylene), play a limited role in the subsequent crystallization due to the short propylene sequence lengths present in the chains. Possible phase separation of these fractions will not affect crystallization kinetics. Although not completely possible to exclude phase separation in the melt, we have reasonable arguments to support the hypothesis that the effects on crystallization kinetics are insignificant, and therefore, we do not include this in the model.

Next, the absolute position of $\chi^p_\infty$ can be measured directly from in-situ WAXD and from DSC. The latter requires immediate heating after reaching spacefilling in isothermal conditions, in order to prevent secondary crystallization phenomena to take place. Not all crystallization temperatures are assessable in combination with in-situ X-ray experiments or standard DSC. Therefore, Flash DSC is used for the lower temperature regime. The melting enthalpy after isothermal crystallization can be used to determine the crystallinity under the assumptions that the difference in heat of fusion for $\alpha$- and $\gamma$-crystals can be neglected [33], and that the value is constant over the whole temperature regime. In Fig. 6, the combined results of $\chi^p_\infty$ from X-ray analyses and DSC experiments are shown, where $\Delta Hf = 191[kJ/mol]$ was used, in line with [34]. Notice that the crystallinity is only determined in the regime where solely $\alpha$ and/or $\gamma$ forms.

The experimental data that represent $\chi^p_\infty(T)$ are indicated in Fig. 6. Below 50 $^\circ C$, where mesophase is expected, the experimental data is not considered since the enthalpy required to obtain a crystallinity is unknown and the risk for melting recrystallization phenomena is high. With the $\chi^{CF}_\infty$ fixed, and an indication of the position and shape of $\chi^p_\infty(T)$ on the basis of X-ray and DSC experiments, the position of $\chi^{KIN}_\infty$ can be determined according to Equation (26).

Fig. 6 shows the positions of $\chi^{KIN}_\infty$ and $\chi^p_\infty$ that are found. The values used to parameterize the polynomial, Equation (29), are given in Table 5.

Due to kinetic effects such as crystallizable sequences getting trapped in non-crystalline regions, $\chi^{KIN}_\infty$ increases with temperature. The kinetic effects increase when crystallization temperatures get lower and lamellae get thinner. Moreover, crystallization rates get higher and thus chains get trapped in a less favorable configuration more easily. In the model the same conclusion follows when considering primary crystallization below 80 $^\circ C$. Here, the crystallizable fraction is close to the plateau value and upon subsequent cooling does not govern a significant increase. Therefore, at these lower temperatures the final crystallinity level based on kinematic effects is close to $\chi^p_\infty$ and secondary crystallization is hardly possible. Around $T^0_m$, the kinematic effects should play a limited role, and thus one would in theory end up with a higher crystallinity. Nevertheless, the crystallizable fraction is low, therewith allowing only a small crystallinity to develop. In this regime, the final crystallinity is dominated by the fraction that can participate in the process.

### 5.5. In-situ X-ray results and model validation

WAXD and SAXS patterns were recorded to follow the structure development during the application of the thermal protocols as depicted in Fig. 7.

To determine time resolved structural features such as the long period and the crystallinity, the isotropic 2D patterns are radially integrated. In Figure 22 of the Supplementary Material, a typical example obtained from the SAXS measurements is presented. Similarly, Fig. 22b depicts a typical corresponding result obtained from the in-situ WAXD experiments. The red curves depict the evolution during the cooling, subsequent to isothermal crystallization until full spacefilling is reached. An obvious change of the maximum in the Lorentz corrected SAXS data can be observed in this part of the experiment.

The evolution of the long period, determined according to Equation (41), is depicted in Fig. 8. Initially, at the onset of crystallization, the long period is large, but with increasing spacefilling, the average decreases and converges to a nearly constant value, specific for that temperature and used to construct Fig. 5b. After the isothermal step, at the onset of cooling, the long period decreases further until it reaches at room temperature approximately the same value for all experiments, independent of the isothermal crystallization temperature at which spacefiling took place. The long period during the cooling step after isothermal crystallization up to full spacefilling is plotted as a function of temperature, see Fig. 8b. Three distinct regimes can be identified in which the long period decreases. The first one, just below the isothermal temperature is the result from thermal shrinkage of (mainly) the amorphous layers. The slope is steeper for higher crystallization temperatures and thus for a larger amorphous content (Fig. 9a). Next, a steeper drop takes place which is resulting from lamellar insertion, similar to Ref. [56]. This drop takes place around 20–40 $^\circ C$ below the isothermal crystallization temperature at which full space filling is reached. The thickness of newly formed secondary lamellae needs to be small enough to fit in the amorphous domains, preserved in the spheruletic skeletons. Eventually, in the third regime below 70 $^\circ C$, the decrease in the long period results from thermal shrinkage again, and due to the (slightly) higher crystallinity the temperature dependence is not as pronounced as in the first regime. If primary crystallization takes

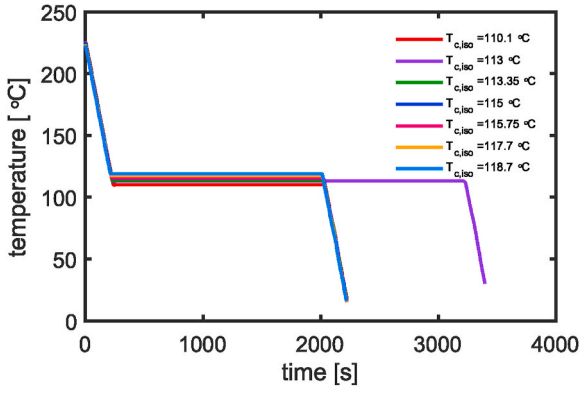


**Fig. 7.** The time temperature profiles of the experiments, carried out at various isothermal crystallization temperatures in combination with in-situ X-ray. The longer experimental time used for $T_{c,iso} = 113^\circ C$ is due to experimental circumstances.

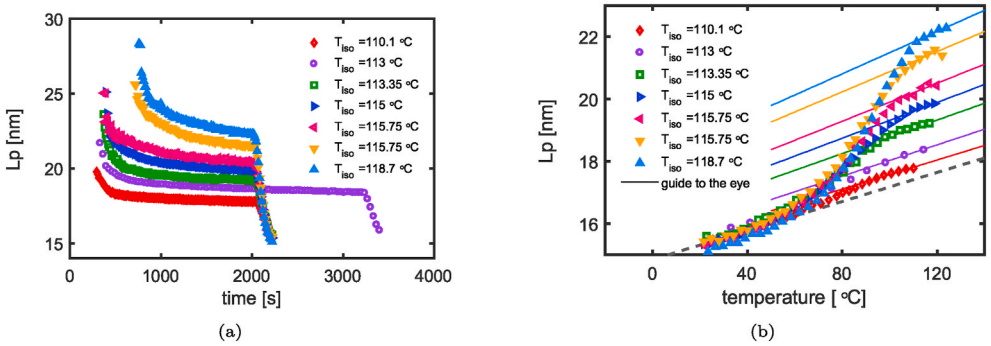


**Fig. 8.** a) The long period as a function of time, calculated according to Equation (41) and applied to experiments with isothermal crystallization at various temperatures. b) The long period as a function of temperature in the cooling step after isothermal crystallization up to full space filling. The strong decrease between 70 and 110 $^{\circ}C$ is attributed to lamellar insertion. Lines are guides to the eye.

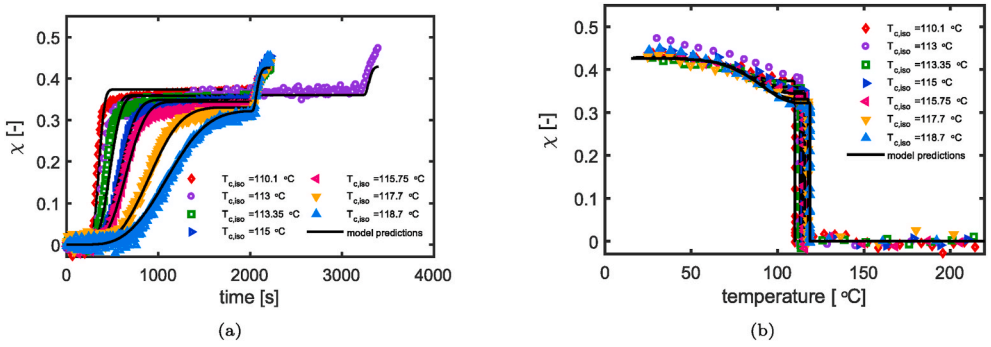


**Fig. 9.** a) The evolution of the crystallinity, obtained from in-situ synchrotron X-ray experiments, as a function of time for the different thermal protocols, see Fig. 7. The markers are the experimental data and the solid lines are the model predictions. b) The same experimental data and model predictions of the crystallinity as a function of temperature.

place at lower temperatures, the available space and material for secondary crystallization phenomena reduces further and further.

The lamellar insertion, a purely secondary phenomenon, has to come along with an increase in crystallinity. Crystallization at high temperatures (above 100$^{\circ}C$) is only possible for the highly isotactic fractions of the material, which will be extracted from the melt and incorporated in the crystal lattice. As a result, the left-over amorphous fraction which crystallizes by means of lamellar insertion upon cooling, contains increased amounts of defects, favoring $\gamma$-iPP formation. Higher crystallization temperatures result in lower primary crystallinity levels, but also in the extraction of the longest propene sequence lengths. Consequently, in all cases predominantly $\gamma$-crystals are formed during secondary crystallization. The higher the crystallization temperatures, the larger the fractions of left over amorphous material and the larger the amount of inserted lamellae. Lamellar perfectioning and thickening of the primary lammellae, typically observed upon annealing at high temperature [75,100], is not included in the model.

Fig. 9 shows the development of the crystallinity $\chi$ as a function of the time-temperature history. In Fig. 9b, part of the experimental data is excluded from the figure for clarity arguments. The markers indicate the experimental outcome, and the solid lines are the model predictions. These predictions consist of a primary part, for which the model parameters are determined and summarized in Table 2, and a secondary part for which the optimal parameters are determined on the basis of in-situ WAXD results. The parameters, aiming for an optimal match between model predictions and experimental results in isothermal and continuous cooling experiments, are summarized in Table 6.

Deconvolution of the WAXD patterns provides detailed information of the phase composition, see Fig. 10. In the predominantly primary isothermal crystallization step, the amount of $\alpha$ increases with decreasing crystallization temperature. For all thermal protocols, a similar absolute amount of $\alpha$ is formed in the secondary crystallization step upon cooling (after reaching full spacefilling at isothermal conditions), see Fig. 11a. The $\gamma$-phase on the other hand gets higher with increasing crystallization temperature, and significantly grows during secondary crystallization. Therefore, the kinetics of $\gamma$ crystal growth are faster than the kinetics of $\alpha$ growth during secondary crystallization, which is in line with the expectations [42,101]. In Table 6, only $\alpha$- and $\gamma$-phase are considered since the other crystal phases did not form in secondary processes. Using these parameters results in the model descriptions, indicated with the black lines in Figs. 9–11. All predictions, as a function of both time (Fig. 10) and temperature (Fig. 11, part of the data excluded from the figure for clarity arguments) of the primary and secondary crystallization phenomena give an accurate description of the experimental results. Moreover, the ratio between $\alpha$- and $\gamma$ polymorphs is captured very well throughout the entire crystallization process.

**Table 6**
Model parameters for the secondary crystallization kinetics.

| Parameter | $i = \alpha$ | $i = \gamma$ | Unit |
|---|---|---|---|
| $a_j$ | 0.7 | 2.135 | $[1/s]$ |
| $T_{ref,j}$ | 340.5 | 344.45 | $[K]$ |
| $b_j$ | 120 | 120 | $[-]$ |
| $n_j$ | 3 | 3 | $[-]$ |

To verify that continuous cooling experiments can be described equally well with this set of parameters, a set of in-situ X-ray experiments conducted on an in-house lab setup, are used (cooling protocol given in Figure 16b), see the results in Figs. 12 and 13. Again, for the three cooling rates investigated here, the model accurately predicts the development of crystals over time and temperature. The crystallization onset time and temperature are predicted well and, moreover, the

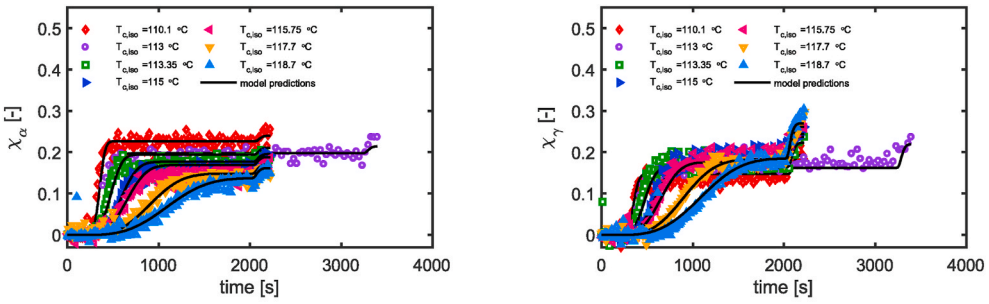


**Fig. 10.** a) The evolution of the $\alpha$-crystal fraction as a function of time, obtained via deconvolution of the WAXD signals recorded from in-situ experiments, measured during the thermal histories shown in Fig. 7 b) The corresponding evolution of the $\gamma$ polymorph.

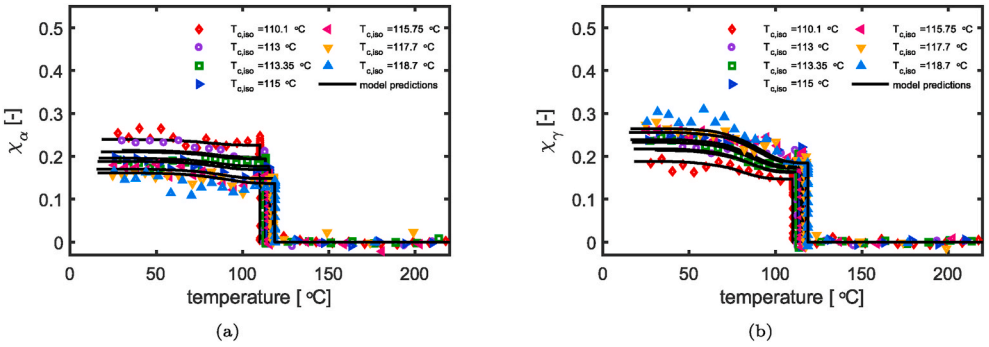


**Fig. 11.** a) The evolution of the $\alpha$-crystal fraction as a function of the temperature, obtained via deconvolution of the WAXD signals recorded from in-situ experiments, measured during the thermal histories shown in Fig. 7 b) The corresponding evolution of the $\gamma$ polymorph.

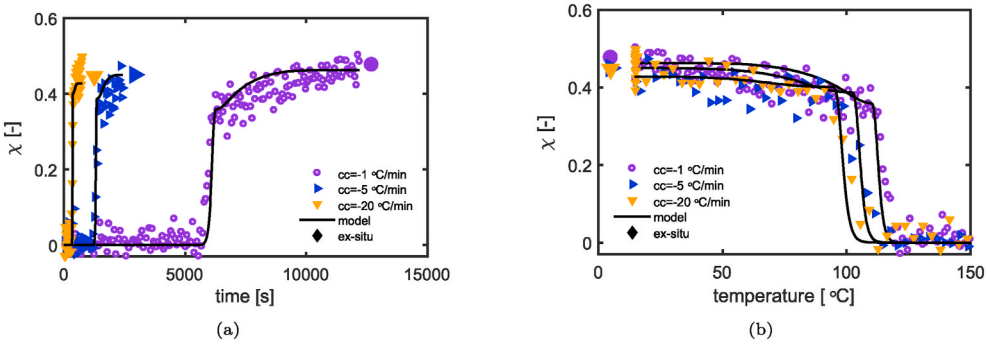


**Fig. 12.** a) The evolution of the crystallinity, obtained from in-situ X-ray experiments, as a function of time, collected simultaneously with the application of continuous cooling rates of 1–5 and 20 °C/min, see Fig. 16b for the cooling procedure. The markers are experimental data and the solid lines are the model predictions. Solid filled markers are obtained from ex-situ X-ray. b) The corresponding evolution of crystallinity as a function of temperature.

structure development until reaching the final temperature is also captured quite well. The lower the cooling rate, the higher the crystallization temperature and the higher the final crystallinity level (combination of primary and secondary). Since the experimental error on the measurements conducted on the lab setup is slightly larger, particularly for the experiments conducted at cooling rates of −20 °C/min, ex-situ experiments were carried out to confirm these final levels, indicated by the solid filled marker in Fig. 12. Moreover, that data is presented starting from a negative crystallinity to show the experimental noise at high temperatures, where the crystallinity is still zero.

A distinction between the $\alpha$- and $\gamma$-phase development can be made in the same way as before, and as evidenced by Fig. 13 (as a function of time and temperature), the model captures the experiments very well. With increasing cooling rate, an growing amount of $\alpha$ crystals is found, while the amount of $\gamma$ crystals decreases. During secondary crystallization, the majority of newly formed crystals are formed in the $\gamma$-phase. Deviations are observed mainly for the experiments carried out at cooling rates of −20 °C/min, which should be attributed to experimental noise.

### 5.6. Model applicability in an extended processing window

It is demonstrated that the model is capable of predicting multiphase structure development in both isothermal crystallization experiments followed by cooling, and continuous cooling experiments. The crystallization half time diagram, depicted in Fig. 14a, is constructed from the inverse crystallization half times, depicted in Fig. 20b, at isothermal conditions over a broad range of temperatures. The solid black line in Fig. 14a represents the model prediction. In both the homogeneous and heterogeneous nucleation regime, the model describes the experimental

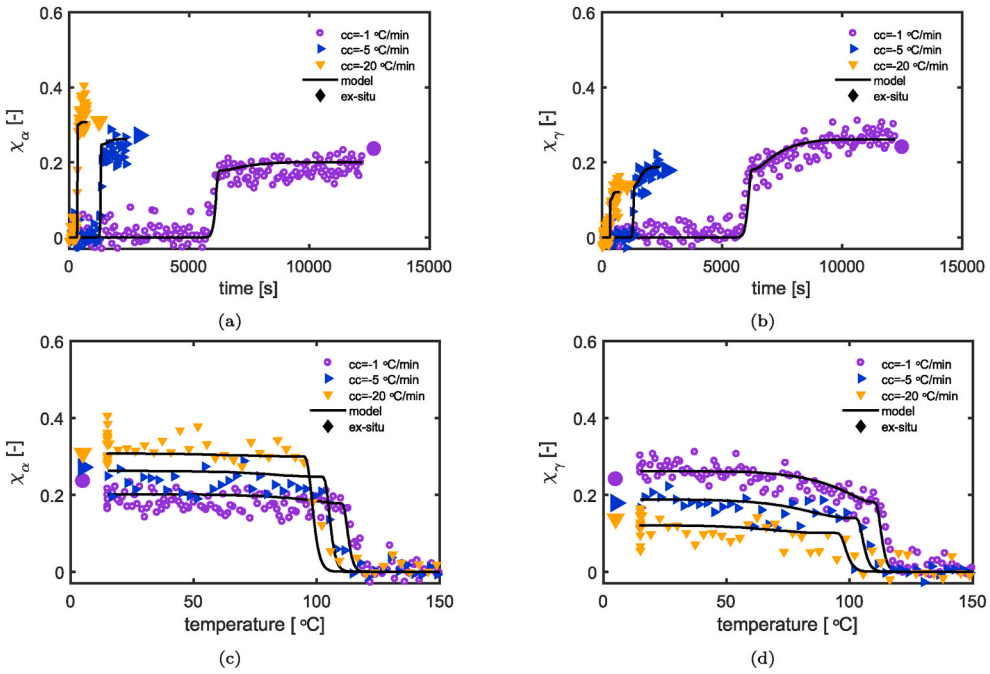


**Fig. 13.** a) The evolution of the alpha crystallinity, obtained from deconvolution of in-situ X-ray experiments, as a function of time, collected simultaneously with the application of continuous cooling rates of 1, 5 and 20 °C/min, see Fig. 16b for the cooling procedure. The markers are experimental data and the solid lines are the model predictions. Solid filled markers are obtained from ex-situ X-ray. b) The corresponding evolution of the gamma crystallinity. c) The evolution of the alpha crystallinity as a function of temperature. d) The corresponding evolution of the gamma crystallinity.

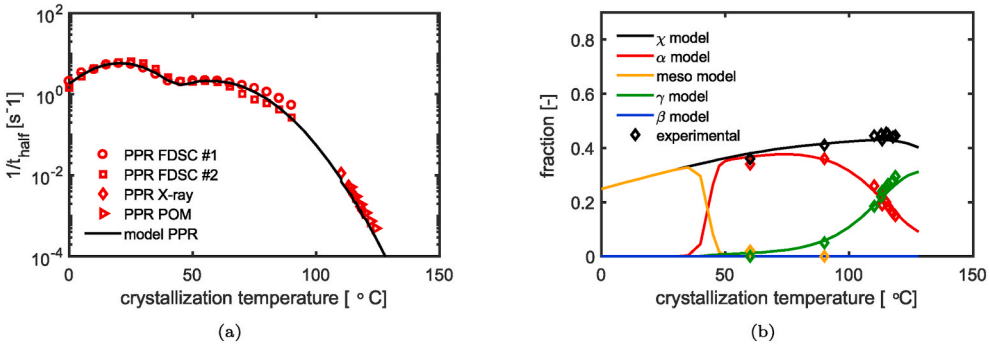


**Fig. 14.** a) Crystallization half times obtained from DSC, X-ray and POM experiments as a function of the isothermal crystallization temperature (markers) and the corresponding model predictions (solid black line). b) The final crystallinity (i.e. at room temperature) and the phase composition resulting from isothermal crystallization at several temperatures determined experimentally (markers), and the corresponding model predictions over a wide range of isothermal crystallization temperatures.

data very well. Fig. 14b shows that phase composition of $\alpha$ and $\gamma$ is properly predicted for the temperatures where it could be verified based on WAXD experiments. Moreover, the level of the final crystallinity within the isothermal step matches the experimentally obtained ones.

A similar plot can be made for the continuous cooling experiments. Also here, the temperature range in which a constant cooling rate could be applied, and for which the samples could be used for X-ray experiments, is rather limited. However, combining Flash DSC and standard DSC data, and scaling to the crystallinity level as obtained by X-ray at low cooling rates, allows to determine the final level of the crystallinity over a broader range, see Fig. 15. Phase composition and the final level of the crystallinity are predicted rather well. In the range in which the transition from mesophase to $\alpha$-phase is found, the predicted crystallinity level is slightly too high. A possible explanation could be that the model predicts a volume percentage of crystals, whereas the Flash DSC gives the crystallinity based on latent heat release. The mesophase and the $\alpha$-phase in this regime are thermally less stable and have a lower heat of fusion. Therefore, latent heat might be scaled with a different factor than the $\alpha$- and $\gamma$-phase to properly translate to a volume percentage. The levels of mesophase that are found in a rather narow range of cooling rates are lower than expected from ballistic cooling experiments [38]. Nevertheless, the results are in agreement with observations on random copolymers of propene and higher $\alpha$-olefins, investigated in continuous cooling experiments [102].

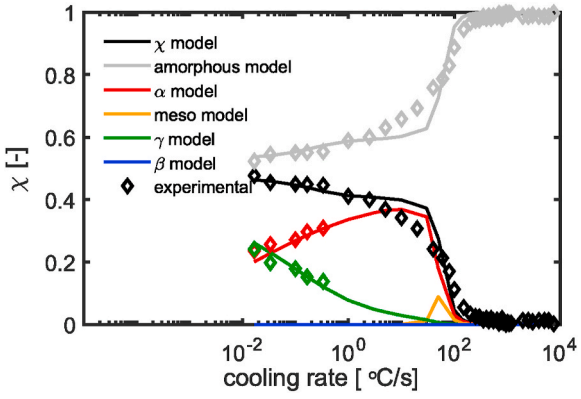


**Fig. 15.** The crystallinity and phase composition as a function of the applied continuous cooling rate, obtained from experiments (markers) and model predictions (solid lines). The melting enthalpy of all crystal phases is assumed to be the same.

## 6. Conclusion

The crystallization behavior of a PP random copolymer has been studied and quantified over a wide range of cooling rates and thermal

protocols by means of (time resolved in-situ) WAXD and SAXS, polarized optical microscopy and (Flash) DSC. Important phenomena like primary and secondary multiphase crystallization and crystallization under isothermal and non-isothermal conditions are quantified.

Based on the experimental information, a previously developed multiphase primary crystallization model is parameterized for a propylene-ethylene random copolymer. Additionally, the existing framework is extended to multiphase secondary crystallization. This extension is based on a concept of a temperature dependent maximum crystallinity level, making the model capable to predict final crystallinity levels as well. The maximum crystallinity is based on the kinetic maximum crystallinity at given temperature on one hand, and on the crystallizable fraction at that temperature on the other hand. In isothermal conditions, the crystallinity develops until reaching the product of the two. However, upon cooling the crystallizable fraction increases, allowing for a further secondary increase of the crystallinity which is predominantly governed by $\gamma$-phase formation.

Parameterization of the secondary crystallization model proceeded via fractionation of the PPR. To determine the crystallizable fraction as a function of temperature, each fraction is studied in $^{13}C$ NMR, to obtain the average regular sequence length. Under the assumption that ethylene does not incorporate in the polypropylene crystals, the fraction that can form a certain lamellar thickness and thus crystallize at a given undercooling is determined. As such, the chemical composition distribution is used as a direct input for the crystallization model proposed in this work. Time-resolved X-ray is used to manually optimize the parameters for the kinetics of the secondary crystallization phenomena on the basis of numerical experiments.

The proposed model framework accurately describes multiphase primary and secondary crystallization phenomena in both isothermal and non-isothermal conditions over a wide range of crystallization temperatures and cooling rates. Deconvolution of the in-situ X-ray revealed an excellent agreement between predicted and experimentally obtained phase composition as a function of time and temperature. The model shows how the chemical composition distribution of ethylene units in propylene chains can be used to understand the crystallization behavior, and to model the final crystallinity and phase composition. Moreover, the framework has proven to be predictive in a quantitative way in processing relevant cooling conditions. To predict structure development in real processing conditions, the model should be extended further to allow for flow induced crystallization predictions. Flow plays an important role in the majority of industrial production processes, and is therefore a topic for future work.

## CRediT authorship contribution statement

**Harm J.M. Caelers:** Conceptualization, Methodology, Software, Writing – original draft, Visualization, Project administration, Formal analysis. **Anke de Cock:** Conceptualization, Methodology, Software, Writing – review & editing. **Stan F.S.P. Looijmans:** Writing – review & editing, Data curation. **Ralf Kleppinger:** Writing – review & editing, Data curation. **Enrico M. Troisi:** Conceptualization, Writing – review & editing. **Martin van Drongelen:** Writing – review & editing, Data curation. **Gerrit W.M. Peters:** Conceptualization, Methodology, Writing – review & editing.

## Declaration of competing interest

The authors declare that they have no known competing financial interests or personal relationships that could have appeared to influence the work reported in this paper.

## Acknowledgments

The time resolved SAXS and WAXD expriments were carried out at the Dutch-Belgian beamline DUBBLE, Grenoble, France. We thank the beamline staff for their assistance in performing the experiments. Moreover, the authors would like to thank Felipe M. Costa and Ismaail A. Emara for their contribution to the execution and analysis of the experiments. Finally, Maria Soliman and Bhaskar Patham are gratefully acknowledged for the useful discussions and financial support.

## Appendix A. Supplementary data

Supplementary data to this article can be found online at https://doi.org/10.1016/j.polymer.2022.124901.

## References

[1] K. Ziegler, E. Holzkamp, H. Breil, H. Martin, Polymerisation von Äthylen und anderen olefinen, 426–426, Angew. Chem. 67 (16) (1955), https://doi.org/10.1002/ange.19550671610.

[2] G. Natta, Une nouvelle classe de polymeres d'$\alpha$-olefines ayant une régularité de structure exceptionnelle, arXiv: J. Polym. Sci. 16 (82) (1955) 143–154, https://doi.org/10.1002/pol.1955.120168205.

[3] D. Mileva, D. Tranchida, M. Gahleitner, Polymer Crystallization 1 (2), cited By 26. doi:10.1002/pcr2.10009. URL https://www.scopus.com/inward/record.uri?eid=2-s2.0-85063683777&doi=10.1002%2fpcr2.10009&partnerID=40&md5=4c3578652e9272e3d338cb504438d594.

[4] M. Gahleitner, P. Jääskeläinen, E. Ratajski, C. Paulik, J. Reussner, J. Wolfschwenger, W. Neißl, J. Appl. Polym. Sci. 95 (5) (2005) 1073–1081, https://doi.org/10.1002/app.21308, cited By 98. doi: https://www.scopus.com/inward/record.uri?eid=2-s2.0-13844298255&doi=10.1002%2fapp.21308&partnerID=40&md5=3bde16d3cc91d013a87d9b51aa8c088a.

[5] J.-W. Housmans, M. Gahleitner, G.W.M. Peters, H.E.H. Meijer, Structure–property relations in molded, nucleated isotactic polypropylene, Polymer 50 (2009) 2304–2319, https://doi.org/10.1016/j.polymer.2009.02.050.

[6] M. Gahleitner, J. Wolfschwenger, C. Bachner, K. Bernreitner, W. Neissl, J. Appl. Polym. Sci. 61 (4) (1996) 649–657, https://doi.org/10.1002/(SICI)1097-4628(19960725)61:4<649::AID-APP8>3.0.CO;2-L, cited By 96, https://www.scopus.com/inward/record.uri?eid=2-s2.0-0030195373&doi=10.1002%2f%28SICI%291097-4628%2819960725%2961%3a4%3c649%3a%3aAID-APP8%3e3.0.CO%3b2-L&partnerID=40&md5=57640e6d1bfd2971b48e53858b658a96.

[7] M. Gahleitner, C. Bachner, E. Ratajski, G. Rohaczek, W. Neißl, J. Appl. Polym. Sci. 73 (12) (1999) 2507–2516, https://doi.org/10.1002/(SICI)1097-4628(19990919)73:12<2507::AID-APP19>3.0.CO;2-V, cited By 43, https://www.scopus.com/inward/record.uri?eid=2-s2.0-0033331817&doi=10.1002%2f%28SICI%291097-4628%2819990919%2973%3a12%3c2507%3a%3aAID-APP19%3e3.0.CO%3b2-V&partnerID=40&md5=9591c5d657ffd8226645c79cf65406fb.

[8] P. Roozemond, T. Van Erp, G. Peters, Polymer (United Kingdom) 89 (2016) 69–80, https://doi.org/10.1016/j.polymer.2016.01.032. https://www.scopus.com/inward/record.uri?eid=2-s2.0-84959260291&doi=10.1016%2fj.polymer.2016.01.032&partnerID=40&md5=5938f43369d437c5eeb5af026d5286f1.

[9] S. Brückner, S. Meille, V. Petraccone, B. Pirozzi, Prog. Polym. Sci. 16 (2–3) (1991) 361–404, https://doi.org/10.1016/0079-6700(91)90023-E. https://www.scopus.com/inward/record.uri?eid=2-s2.0-0025813732&doi=10.1016%2f0079-6700%2891%2990023-E&partnerID=40&md5=771ac3637ef31e8e536a3f2b71dabcf2.

[10] B. Lotz, J. Wittmann, A. Lovinger, Polymer 37 (22) (1996) 4979–4992, https://doi.org/10.1016/0032-3861(96)00370-9, cited By 535, https://www.scopus.com/inward/record.uri?eid=2-s2.0-0030259631&doi=10.1016%2f0032-3861%2896%2900370-9&partnerID=40&md5=483126292b179cd31597597e9a2c039b.

[11] H. J. M. Caelers, E. Parodi, D. Cavallo, G. W. M. Peters, L. E. Govaert, Deformation and failure kinetics of ipp polymorphs., J. Polym. Sci. B Polym. Phys.:10.1002/polb.24325.

[12] J. Varga, β-modification of isotactic polypropylene: preparation, structure, processing, properties, and application, J. Macromol. Sci. Part B: Physics 41 (2002) 1121–1171, https://doi.org/10.1081/MB-120013089.

[13] B. Schrauwen, R. Janssen, L. Govaert, H. Meijer, Intrinsic deformation behavior of semicrystalline polymers, Macromolecules 37 (16) (2004) 6069–6078. http://www.scopus.com/inward/record.url?eid=2-s2.0-4344638041&partnerID=40&md5=6dc7401ff5b104cb05dfcac31ba70c20.

[14] C. De Rosa, F. Auriemma, R. Di Girolamo, O. De Ballesteros, M. Pepe, O. Tarallo, A. Malafronte, Macromolecules 46 (13) (2013) 5202–5214, https://doi.org/10.1021/ma400570k. https://www.scopus.com/inward/record.uri?eid=2-s2.0-84880149474&doi=10.1021%2fma400570k&partnerID=40&md5=d6a14d5a811fe78b6b2c64c99330371a.

[15] Y. Cohen, R. Saraf, Polymer 42 (13) (2001) 5865–5870, https://doi.org/10.1016/S0032-3861(00)00914-9, cited By 29, https://www.scopus.com/inward/record.uri?eid=2-s2.0-0035970499&doi=10.1016%2fS0032-3861%2800%2900914-9&partnerID=40&md5=f9b9606ccaef571ad61aa36e288c59bf.

[16] S. Valdo Meille, S. Brückner, Non-parallel chains in crystalline $\gamma$-isotactic polypropylene, Nature 340 (6233) (1989) 455–457. http://www.scopus.com/inward/record.url?eid=2-s2.0-36849149716&partnerID=40&md5=6b989fd4426c276c9f4a25637f3defcb.

[17] K. Mezghani, P. Phillips, The $\gamma$-phase of high molecular weight isotactic polypropylene. ii: the morphology of the $\gamma$-form crystallized at 200 mpa, Polymer

38 (23) (1997) 5725–5733, cited By 80. URL, https://www.scopus.com/inward/record.uri?eid=2-s2.0-0031270968&partnerID=40&md5=a7931a6052b9f1eb235c2351080d53fd.

[18] L. Zhang, M. Van Drongelen, G. Alfonso, G. Peters, Eur. Polym. J. 71 (2015) 185–195, https://doi.org/10.1016/j.eurpolymj.2015.07.055, cited By 11, https://www.scopus.com/inward/record.uri?eid=2-s2.0-84955572334&doi=10.1016%2fj.eurpolymj.2015.07.055&partnerID=40&md5=88b4c722d1fc570175d102a343dafac2.

[19] C. De Rosa, F. Auriemma, A. Di Capua, L. Resconi, S. Guidotti, I. Camurati, I. Nifant'ev, I. Laishevtsev, Structure-property correlations in polypropylene from metallocene catalysts: stereodefective, regioregular isotactic polypropylene, J. Am. Chem. Soc. 126 (51) (2004) 17040–17049, https://doi.org/10.1021/ja045684f. http://www.scopus.com/inward/record.url?eid=2-s2.0-11244353378&partnerID=40&md5=e5a7d6ce6a10238ee5dbdb6b360baf55.

[20] D.R. Morrow, B.A. Newman, Crystallization of low-molecular-weight polypropylene fractions, arXiv: J. Appl. Phys. 39 (11) (1968) 4944–4950, https://doi.org/10.1063/1.1655891.

[21] H. Zimmermann, J. Macromol. Sci., Part B 32 (2) (1993) 141–161, https://doi.org/10.1080/00222349308215477, cited By 50, https://www.scopus.com/inward/record.uri?eid=2-s2.0-0027242726&doi=10.1080%2f00222349308215477&partnerID=40&md5=5f6f999c81d5a171deca741caa27dec3.

[22] R. Alamo, A. Ghosal, J. Chatterjee, K. Thompson, Polymer 46 (20) (2005) 8774–8789, https://doi.org/10.1016/j.polymer.2005.02.128, cited By 54, https://www.scopus.com/inward/record.uri?eid=2-s2.0-24144469141&doi=10.1016%2fj.polymer.2005.02.128&partnerID=40&md5=7671587d3dee12826158a56a5fe993d3.

[23] S. Meille, D. Ferro, S. Brückner, A. Lovinger, F. Padden, Structure of $\beta$-isotactic polypropylene: a long-standing structural puzzle, Macromolecules 27 (9) (1994) 2615–2622. http://www.scopus.com/inward/record.url?eid=2-s2.0-0028419063&partnerID=40&md5=64a1ae86b67e3b2248c0d4b33095feeb.

[24] J. Varga, I. Mudra, G. Ehrenstein, Highly active thermally stable $\beta$-nucleating agents for isotactic polypropylene, J. Appl. Polym. Sci. 74 (10) (1999) 2357–2368, https://doi.org/10.1002/(SICI)1097-4628(19991205)74:10<2357::AID-APP3>3.0.CO;2-2. http://www.scopus.com/inward/record.url?eid=2-s2.0-0032596076&partnerID=40&md5=f41fbaa8a38e127034e94a1cfed11f90.

[25] J. Varga, J. Karger-Kocsis, Rules of supermolecular structure formation in sheared isotactic polypropylene melts, J. Polym. Sci. B Polym. Phys. 34 (4) (1996) 657–670. http://www.scopus.com/inward/record.url?eid=2-s2.0-0005254361&partnerID=40&md5=a5e0e452d928a40d2f9ad21763f39ca0.

[26] B.A.G. Schrauwen, L.C.A. van Breemen, A.B. Spoelstra, L.E. Govaert, G.W. M. Peters, H.E.H. Meijer, Structure, deformation, and failure of flow-oriented semicrystalline polymers, Macromolecules 37 (2004) 8618–8633, https://doi.org/10.1021/ma048884k.

[27] T. Van Erp, C. Reynolds, T. Peijs, J. Van Dommelen, L. Govaert, J. Polym. Sci. B Polym. Phys. 47 (20) (2009) 2026–2035, https://doi.org/10.1002/polb.21801, cited By 53. doi, https://www.scopus.com/inward/record.uri?eid=2-s2.0-70349775835&doi=10.1002%2fpolb.21801&partnerID=40&md5=789f6ae8fcfa510ab14fa6b24b907a35.

[28] G. Grosso, E.M. Troisi, N.O. Jaensson, G.W.M. Peters, P.D. Anderson, Modelling flow induced crystallization of iPP: multiple crystal phases and morphologies, Polymer 182 (2019), 121806, https://doi.org/10.1016/j.polymer.2019.121806.

[29] E. Troisi, H. Caelers, G. Peters, Macromolecules 50 (10) (2017) 3868–3882, https://doi.org/10.1021/acs.macromol.7b00595, cited By 25, https://www.scopus.com/inward/record.uri?eid=2-s2.0-85019862372&doi=10.1021%2facs.macromol.7b00595&partnerID=40&md5=7a4ef67088bb892a5416ac16c479f1b4.

[30] V. Speranza, S. Liparoti, V. Volpe, G. Titomanlio, R. Pantani, Polymer 196, cited By 5. doi:10.1016/j.polymer.2020.122459. URL https://www.scopus.com/inward/record.uri?eid=2-s2.0-85083291559&doi=10.1016%2fj.polymer.2020.122459&partnerID=40&md5=35b7ac4d05152ca7f0a921a235b416db.

[31] L. Zheng, L. Fernandez-Ballester, G. Peters, Z. Ma, Ind. Eng. Chem. Res. 57 (20) (2018) 6870–6877, https://doi.org/10.1021/acs.iecr.8b00708, cited By 6, https://www.scopus.com/inward/record.uri?eid=2-s2.0-85046737052&doi=10.1021%2facs.iecr.8b00708&partnerID=40&md5=50f4c01d631aa42096a47370c5d832df.

[32] C. De Rosa, F. Auriemma, O. De Ballesteros, L. Resconi, I. Camurati, Macromolecules 40 (18) (2007) 6600–6616, https://doi.org/10.1021/ma070409+, cited By 125, https://www.scopus.com/inward/record.uri?eid=2-s2.0-34748832421&doi=10.1021%2fma070409%2b&partnerID=40&md5=c4c4a527d78e213811a5de13f116ccae.

[33] T. Foresta, S. Piccarolo, G. Goldbeck-Wood, Polymer 42 (3) (2001) 1167–1176, https://doi.org/10.1016/S0032-3861(00)00404-3, cited By 122, https://www.scopus.com/inward/record.uri?eid=2-s2.0-0034139505&doi=10.1016%2fS0032-3861%2800%2900404-3&partnerID=40&md5=f4fc6289efcdc499117f250079b6d9a0.

[34] M. Avella, E. Martuscelli, G.D. Volpe, A. Segre, E. Rossi, T. Simonazzi, Composition-properties relationships in propene-ethene random copolymers obtained with high-yield ziegler-natta supported catalysts, Makromol. Chem. 187 (8) (1986) 1927–1943, https://doi.org/10.1002/macp.1986.021870812, arXiv, https://onlinelibrary.wiley.com/doi/pdf/10.1002/macp.1986.021870812.

[35] A. Kamdar, Y. Hu, P. Ansems, S. Chum, A. Hiltner, E. Baer, Macromolecules 39 (4) (2006) 1496–1506, https://doi.org/10.1021/ma052214c, cited By 33, https://www.scopus.com/inward/record.uri?eid=2-s2.0-33644617592&doi=10.1021%2fma052214c&partnerID=40&md5=3d1c2438eb14e0cf452dce6a0cb69129.

[36] M. Van Drongelen, T. Van Erp, G. Peters, Quantification of non-isothermal, multi-phase crystallization of isotactic polypropylene: the influence of cooling rate and pressure, Polymer 53 (21) (2012) 4758–4769, https://doi.org/10.1016/j.polymer.2012.08.003. http://www.scopus.com/inward/record.url?eid=2-s2.0-84866346528&partnerID=40&md5=c955ba7ac7f06bfd34d8120f378a6500.

[37] K. Nozaki, Y. Endo, T. Yamamoto, M. Naiki, J. Macromol. Sci., Phys. 42 (3–4 SPEC) (2003) 697–707, https://doi.org/10.1081/mb-120021600, cited By 4. doi, https://www.scopus.com/inward/record.uri?eid=2-s2.0-0041930582&doi=10.1081%2fmb-120021600&partnerID=40&md5=0a84b6d65fd81393da308c72fe0dc445.

[38] D. Cavallo, F. Azzurri, R. Floris, G. Alfonso, L. Balzano, G. Peters, Macromolecules 43 (6) (2010) 2890–2896, https://doi.org/10.1021/ma902865e, cited By 57, https://www.scopus.com/inward/record.uri?eid=2-s2.0-77951926778&doi=10.1021%2fma902865e&partnerID=40&md5=1ef47321ed189efce11578fdaa9d7e10.

[39] R. Androsch, M. Di Lorenzo, C. Schick, B. Wunderlich, Polymer 51 (21) (2010) 4639–4662, https://doi.org/10.1016/j.polymer.2010.07.033, cited By 198, https://www.scopus.com/inward/record.uri?eid=2-s2.0-77956929114&doi=10.1016%2fj.polymer.2010.07.033&partnerID=40&md5=0f1c61e39032e0519709301b338cac9b.

[40] J. Schawe, Thermochim. Acta 603 (2015) 85–93, https://doi.org/10.1016/j.tca.2014.11.006, cited By 72, https://www.scopus.com/inward/record.uri?eid=2-s2.0-85027956532&doi=10.1016%2fj.tca.2014.11.006&partnerID=40&md5=cabfd288acf678f338fe6dcc54319ba7.

[41] C. De Rosa, F. Auriemma, T. Circelli, R. Waymouth, Macromolecules 35 (9) (2002) 3622–3629, https://doi.org/10.1021/ma0116248, cited By 78, https://www.scopus.com/inward/record.uri?eid=2-s2.0-0037161402&doi=10.1021%2fma0116248&partnerID=40&md5=d0c1096cad890a44d4658dfbc797fea3.

[42] J. Chen, Y. Cao, J. Kang, H. Li, J. Macromol. Sci., Part B: Physics 50 (2) (2011) 248–265, https://doi.org/10.1080/00222341003648904, cited By 6. doi: https://www.scopus.com/inward/record.uri?eid=2-s2.0-78650330424&doi=10.1080%2f00222341003648904&partnerID=40&md5=a0cae9dadd3add90d9c6c23d8208f324.

[43] I. Hosier, R. Alamo, P. Esteso, J. Isasi, L. Mandelkern, Macromolecules 36 (15) (2003) 5623–5636, https://doi.org/10.1021/ma030157m, cited By 165, https://www.scopus.com/inward/record.uri?eid=2-s2.0-0041701425&doi=10.1021%2fma030157m&partnerID=40&md5=01191cc68651cec262fc7d86c02f5073.

[44] I. Hosier, R. Alamo, J. Lin, Polymer 45 (10) (2004) 3441–3455, https://doi.org/10.1016/j.polymer.2004.02.071, cited By 74, https://www.scopus.com/inward/record.uri?eid=2-s2.0-1942456634&doi=10.1016%2fj.polymer.2004.02.071&partnerID=40&md5=60a19be3854e2d7b9e23e69a560d1fbd.

[45] Q. Gou, L. HuiHui, Z. Yu, E. Chen, Y. Zhang, S. Yan, Chin. Sci. Bull. 53 (12) (2008) 1804–1812, https://doi.org/10.1007/s11434-008-0252-2, cited By 6, https://www.scopus.com/inward/record.uri?eid=2-s2.0-45749096666&doi=10.1007%2fs11434-008-0252-2&partnerID=40&md5=f9af6b2cb236f44a402e0b374731573d.

[46] S. Hild, A. Boger, C. Troll, B. Rieger, Polym. J. 41 (11) (2009) 993–1004, https://doi.org/10.1295/polymj.PJ2008131, cited By 6, https://www.scopus.com/inward/record.uri?eid=2-s2.0-77951699957&doi=10.1295%2fpolymj.PJ2008131&partnerID=40&md5=21642bbf04110432f3cb809aaee04698.

[47] D. Norton, A. Keller, Polymer 26 (5) (1985) 704–716, https://doi.org/10.1016/0032-3861(85)90108-9, cited By 488, https://www.scopus.com/inward/record.uri?eid=2-s2.0-0022059022&doi=10.1016%2f0032-3861%2885%2990108-9&partnerID=40&md5=5a9f97a2d8ab6654d00ff51757600309.

[48] W. Stocker, S. Magonov, H.-J. Cantow, J. Wittmann, B. Lotz, Macromolecules 26 (22) (1993) 5915–5923, https://doi.org/10.1021/ma00074a013, cited By 105, https://www.scopus.com/inward/record.uri?eid=2-s2.0-0027683152&doi=10.1021%2fma00074a013&partnerID=40&md5=cf2c28d6aa06eed12a340e8082fbea03.

[49] D. van der Meer, J. Varga, G. Vancso, Express Polym. Lett. 9 (3) (2015) 233–254, https://doi.org/10.3144/expresspolymlett.2015.23, cited By 12, https://www.scopus.com/inward/record.uri?eid=2-s2.0-84922024004&doi=10.3144%2fexpresspolymlett.2015.23&partnerID=40&md5=2ab3dc2af871ad8f4a0e646986d64c46.

[50] R. Androsch, A. Monami, J. Kucera, J. Cryst. Growth 408 (2014) 91–96, https://doi.org/10.1016/j.jcrysgro.2014.09.028, cited By 23, https://www.scopus.com/inward/record.uri?eid=2-s2.0-84908030283&doi=10.1016%2fj.jcrysgro.2014.09.028&partnerID=40&md5=f3bce6aa6eed4fb131f00f0d8efda5b8.

[51] M. Gahleitner, C. Grein, S. Kheirandish, J. Wolfschwenger, Int. Polym. Process. 26 (1) (2011), https://doi.org/10.3139/217.2411, 2–20, cited By 81, https://www.scopus.com/inward/record.uri?eid=2-s2.0-84860456703&doi=10.3139%2f217.2411&partnerID=40&md5=a43804a7570775845a3420a56589c371.

[52] C. Schick, R. Androsch, Polymer Crystallization 1 (4), cited By 12. doi:10.1002/pcr2.10036. URL https://www.scopus.com/inward/record.uri?eid=2-s2.0-85089978160&doi=10.1002%2fpcr2.10036&partnerID=40&md5=d1185c38127b94a6283befde1e6d7135.

[53] D. Mileva, R. Androsch, E. Zhuravlev, C. Schick, B. Wunderlich, Polymer 53 (2) (2012) 277–282, https://doi.org/10.1016/j.polymer.2011.11.064, cited By 65, https://www.scopus.com/inward/record.uri?eid=2-s2.0-84855852858&doi=10.1016%2fj.polymer.2011.11.064&partnerID=40&md5=e47a6e4986097c8e091cecde5d6c11c5.

[54] E. Troisi, S. Arntz, P. Roozemond, A. Tsou, G. Peters, Eur. Polym. J. 97 (2017) 397–408, https://doi.org/10.1016/j.eurpolymj.2017.09.042, cited By 4, https://www.scopus.com/inward/record.uri?eid=2-s2.0-85032678053&doi=10.

1016%2fj.eurpolymj.2017.09.042&partnerID=40&md5=cbd5de721abeaeb901d146eb79159aa4.
[55] F. Paolucci, D. Baeten, P. Roozemond, B. Goderis, G. Peters, Polymer 155 (2018) 187–198, https://doi.org/10.1016/j.polymer.2018.09.037, cited By 16, https://www.scopus.com/inward/record.uri?eid=2-s2.0-85054067077&doi=10.1016%2fj.polymer.2018.09.037&partnerID=40&md5=36bad4b567baf61fb60eb3f7f1477b3d.
[56] F. Auriemma, O. Ruiz de Ballesteros, G. Giusto, R. Di Girolamo, A. Malafronte, M. Scoti, C. De Rosa, G. Mitchell, Polymer 215, cited By 0. doi:10.1016/j.polymer.2021.123411. URL https://www.scopus.com/inward/record.uri?eid=2-s2.0-85099513135&doi=10.1016%2fj.polymer.2021.123411&partnerID=40&md5=6e2eebe1cde2e8e7f9d7341728477f87.
[57] F. Auriemma, O. Ruiz De Ballesteros, C. De Rosa, C. Invigorito, Macromolecules 44 (15) (2011) 6026–6038, https://doi.org/10.1021/ma201420f, cited By 12, https://www.scopus.com/inward/record.uri?eid=2-s2.0-79961054767&doi=10.1021%2fma201420f&partnerID=40&md5=dbc923a00cfa19a0528d7dfc99deccf9.
[58] M. Van Drongelen, P. Roozemond, E. Troisi, A. Doufas, G. Peters, Polymer 76 (2015) 254–270, https://doi.org/10.1016/j.polymer.2015.09.010, cited By 13, https://www.scopus.com/inward/record.uri?eid=2-s2.0-84942084038&doi=10.1016%2fj.polymer.2015.09.010&partnerID=40&md5=7bde3c5c4729f45a0ea6d3b25e04c3f1.
[59] N. Yaghini, G.W.M. Peters, Modeling crystallization kinetics and resulting properties of polyamide 6, Macromolecules 54 (4) (2021) 1894–1904, https://doi.org/10.1021/acs.macromol.0c02588.
[60] R. Alamo, M.-H. Kim, M. Galante, J. Isasi, L. Mandelkern, Macromolecules 32 (12) (1999) 4050–4064, https://doi.org/10.1021/ma981849r, cited By 205, https://www.scopus.com/inward/record.uri?eid=2-s2.0-0032681095&doi=10.1021%2fma981849r&partnerID=40&md5=00e32a95772c41a15d3eada8470139b8.
[61] A. Toda, R. Androsch, C. Schick, Polymer 91 (2016) 239–263, https://doi.org/10.1016/j.polymer.2016.03.038, cited By 131, https://www.scopus.com/inward/record.uri?eid=2-s2.0-84979462422&doi=10.1016%2fj.polymer.2016.03.038&partnerID=40&md5=6cc905c5f67b039c5a66abdaf1f20eff.
[62] R. Alamo, D. Vanderhart, M. Nyden, L. Mandelkern, Morphological partitioning of ethylene defects in random propylene-ethylene copolymers, Macromolecules 33 (16) (2000) 6106–6119, cited By 1. URL, https://www.scopus.com/inward/record.uri?eid=2-s2.0-33749147436&partnerID=40&md5=8702535a7fc7aee192555f178c2eaf7a.
[63] J.I.J. Lauritzen, H.J. D, Theory of formation of polymer crystals with folded chains in dilute solution, J. Res. Natl Bureau Stand. Sect. A, Phys. Chem. 1 (64A) (1960) 73–102, https://doi.org/10.6028/jres.064A.007.
[64] J.D. Hoffman, J.I.J. Lauritzen, Crystallization of bulk polymers with chain folding: theory of growth of lamellar spherulites, J. Res. Natl Bureau Stand. Sect. A, Phys. Chem. 4 (65A) (1961) 297–336, https://doi.org/10.6028/jres.065A.035.
[65] J. Lauritzen Jr., J. Hoffman, Extension of theory of growth of chain-folded polymer crystals to large undercoolings, J. Appl. Phys. 44 (10) (1973) 4340–4352, https://doi.org/10.1063/1.1661962. http://www.scopus.com/inward/record.url?eid=2-s2.0-0015672949&partnerID=40&md5=3a0333f8433d4d744ab55d01a46cb568.
[66] J.D. Hoffman, J. Weeks, J. Chem. Phys. 37 (8) (1962) 1723–1741, https://doi.org/10.1063/1.1733363, cited by: 347, https://www.scopus.com/inward/record.uri?eid=2-s2.0-51149212912&doi=10.1063%2f1.1733363&partnerID=40&md5=fb319d2ef6eb4e6eb2c931e74906ffaf.
[67] A. Kolmogoroff, On the statistic theory of metal crystallization (in Russian), Izvestiia Akademii Nauk SSSR Ser Math 1 (1937) 335–339.
[68] M. Avrami, Kinetics of phase change. i: general theory, J. Chem. Phys. 7 (12) (1939) 1103–1112. http://www.scopus.com/inward/record.url?eid=2-s2.0-0342869049&partnerID=40&md5=649c2ef3b5c730c668cff7795b9d7685.
[69] M. Avrami, Kinetics of phase change. ii transformation-time relations for random distribution of nuclei, J. Chem. Phys. 8 (2) (1940) 212–224. http://www.scopus.com/inward/record.url?eid=2-s2.0-0001336124&partnerID=40&md5=8a2e91396e9346e2cccb05bd2e0b92b4.
[70] W. Schneider, A. Köppel, J. Berger, Non - isothermal crystallization of polymers, Int. Polymer Process. II (3–4) (1988) 151–154. www.scopus.com.
[71] S. Looijmans, D. Cavallo, L. Yu, G. Peters, Cryst. Growth Des. 18 (7) (2018) 3921–3926, https://doi.org/10.1021/acs.cgd.8b00254, cited By 4. doi: https://www.scopus.com/inward/record.uri?eid=2-s2.0-85048097661&doi=10.1021%2facs.cgd.8b00254&partnerID=40&md5=f216e50dc7fe41cc24cf34d51fb364bd.
[72] J. Koutsky, A. Walton, E. Baer, J. Appl. Phys. 38 (4) (1967) 1832–1839, https://doi.org/10.1063/1.1709769, cited By 173, https://www.scopus.com/inward/record.uri?eid=2-s2.0-36849100001&doi=10.1063%2f1.1709769&partnerID=40&md5=557c127155213dca8383584fb6b4f337.
[73] H. Caelers, L. Govaert, G. Peters, Polymer 83 (2016) 116–128, https://doi.org/10.1016/j.polymer.2015.12.001, cited By 26, https://www.scopus.com/inward/record.uri?eid=2-s2.0-84951949416&doi=10.1016%2fj.polymer.2015.12.001&partnerID=40&md5=96c7a6374957abe16c7aa0f8eab99d9c.
[74] R.J. Cerpentier, M. van Drongelen, T.A. Tervoort, M.J. Boerakker, L.E. Govaert, The Effect of Crystallinity and Lamellar Thickness on the Yield Sress and Young's Modulus of Polyethylene, Eindhoven University of Technology, Department of Mechanical Engineering, 2021. Ph.D. thesis.
[75] J. Xu, S. Srinivas, H. Marand, P. Agarwal, Macromolecules 31 (23) (1998) 8230–8242, https://doi.org/10.1021/ma980748q, cited By 133, https://www.scopus.com/inward/record.uri?eid=2-s2.0-0032203618&doi=10.1021%2fma980748q&partnerID=40&md5=574592fb00bb23ac676a8e394a4f173e.
[76] S. Piccarolo, M. Saiu, V. Brucato, G. Titomanlio, J. Appl. Polym. Sci. 46 (4) (1992) 625–634, https://doi.org/10.1002/app.1992.070460409, cited by: 99, https://www.scopus.com/inward/record.uri?eid=2-s2.0-0027112807&doi=10.1002%2fapp.1992.070460409&partnerID=40&md5=e5dc1e02443daad2a337c34ac85292d7.
[77] J. Janimak, S. Cheng, A. Zhang, E. Hsieh, Polymer 33 (4) (1992) 728–735, https://doi.org/10.1016/0032-3861(92)90329-U, cited By 101, https://www.scopus.com/inward/record.uri?eid=2-s2.0-0343869362&doi=10.1016%2f0032-3861%2892%2990329-U&partnerID=40&md5=05f3a144ae2ed9295d845600a68f4e6a.
[78] W. Bras, I. Dolbnya, D. Detollenaere, R. Van Tol, M. Malfois, G. Greaves, A. Ryan, E. Heeley, Recent experiments on a combined small-angle/wide-angle x-ray scattering beam line at the esrf, J. Appl. Crystallogr. 36 (3 I) (2003) 791–794. http://www.scopus.com/inward/record.url?eid=2-s2.0-0038128355&partnerID=40&md5=1b10e05bd5da4b284d0a15b7cd6fc8fe.
[79] F. De Santis, R. Pantani, J. Therm. Anal. Calorim. 112 (3) (2013) 1481–1488, https://doi.org/10.1007/s10973-012-2732-5, cited By 22, https://www.scopus.com/inward/record.uri?eid=2-s2.0-84878707394&doi=10.1007%2fs10973-012-2732-5&partnerID=40&md5=43b4da4f3da80ea8f08ae249159e52e1.
[80] R. Thomann, C. Wang, J. Kressler, R. Muelhaupt, Macromolecules 29 (26) (1996) 8425–8434, https://doi.org/10.1021/ma951885f, cited By 144, https://www.scopus.com/inward/record.uri?eid=2-s2.0-0030395939&doi=10.1021%2fma951885f&partnerID=40&md5=d00a66b47951cc6f66cfd9ddb54f684c.
[81] H. Janeschitz-Kriegl, E. Ratajski, H. Wippel, Colloid Polym. Sci. 277 (2–3) (1999) 217–226, https://doi.org/10.1007/PL00013746, cited By 81, https://www.scopus.com/inward/record.uri?eid=2-s2.0-0032973275&doi=10.1007%2fPL00013746&partnerID=40&md5=e7c108625ef16c42156ea8ef9f439a3b.
[82] M. Stadlbauer, H. Janeschitz-Kriegl, G. Eder, E. Ratajski, J. Rheol. 48 (3) (2004) 631–639, https://doi.org/10.1122/1.1718542, cited By 71, https://www.scopus.com/inward/record.uri?eid=2-s2.0-3042575349&doi=10.1122%2f1.1718542&partnerID=40&md5=3ab1caac023df71ae8cfdc84fe03b8d3.
[83] I. Coccorullo, R. Pantani, G. Titomanlio, Polymer 44 (1) (2003) 307–318, https://doi.org/10.1016/S0032-3861(02)00762-0, cited by: 110, https://www.scopus.com/inward/record.uri?eid=2-s2.0-0037159849&doi=10.1016%2fS0032-3861%2802%2900762-0&partnerID=40&md5=d90a137f78983c1d430c8c87729993f0.
[84] Z. Ma, R. Steenbakkers, J. Giboz, G. Peters, Rheol. Acta 50 (11–12) (2011) 909–915, https://doi.org/10.1007/s00397-010-0506-1, cited by: 18; All Open Access, Bronze Open Access, https://www.scopus.com/inward/record.uri?eid=2-s2.0-81555214522&doi=10.1007%2fs00397-010-0506-1&partnerID=40&md5=f19029074632a9c15479fbce9057fc02.
[85] H. Janeschitz-Kriegl, G. Eder, M. Stadlbauer, E. Ratajski, Monatshefte fur Chemie 136 (7) (2005) 1119–1137, https://doi.org/10.1007/s00706-005-0328-5, cited by: 22, https://www.scopus.com/inward/record.uri?eid=2-s2.0-21844467229&doi=10.1007%2fs00706-005-0328-5&partnerID=40&md5=2289effbfd30f31a625fb90ad1b3513e.
[86] J. Janimak, S. Cheng, P. Giusti, E. Hsieh, Macromolecules 24 (9) (1991) 2253–2260, https://doi.org/10.1021/ma00009a020, cited By 127, https://www.scopus.com/inward/record.uri?eid=2-s2.0-0026138804&doi=10.1021%2fma00009a020&partnerID=40&md5=9656b5101b47c73f08dabf67a36783fc.
[87] R. Alamo, J. Blanco, P. Agarwal, J. Randall, Macromolecules 36 (5) (2003) 1559–1571, https://doi.org/10.1021/ma021549g, cited By 70, https://www.scopus.com/inward/record.uri?eid=2-s2.0-0037432348&doi=10.1021%2fma021549g&partnerID=40&md5=d2dcf70b1731718f01f3c5a20144aa3e.
[88] G. Lamberti, Polym. Bull. 52 (6) (2004) 443–449, https://doi.org/10.1007/s00289-004-0304-y, cited By 32, https://www.scopus.com/inward/record.uri?eid=2-s2.0-11244256733&doi=10.1007%2fs00289-004-0304-y&partnerID=40&md5=7d595fec4bc4fb12bc1eac55bfc4b54a.
[89] J. Kang, Y. Cao, H. Li, J. Li, S. Chen, F. Yang, M. Xiang, J. Polym. Res. 19 (12), cited By 35. doi:10.1007/s10965-012-0037-9. URL https://www.scopus.com/inward/record.uri?eid=2-s2.0-84869418866&doi=10.1007%2fs10965-012-0037-9&partnerID=40&md5=3404ada7f2181bd8e8ba18a7ce491b95.
[90] J. Kang, J. Li, S. Chen, H. Peng, B. Wang, Y. Cao, H. Li, J. Chen, J. Gai, F. Yang, M. Xiang, J. Appl. Polym. Sci. 129 (5) (2013) 2663–2670, https://doi.org/10.1002/app.38984, cited By 36. doi: https://www.scopus.com/inward/record.uri?eid=2-s2.0-84879409106&doi=10.1002%2fapp.38984&partnerID=40&md5=eb57365f484babad650eeb858e76adf1.
[91] K. Jeon, Y. Chiari, R. Alamo, Macromolecules 41 (1) (2008) 95–108, https://doi.org/10.1021/ma070757b, cited By 44, https://www.scopus.com/inward/record.uri?eid=2-s2.0-39149094277&doi=10.1021%2fma070757b&partnerID=40&md5=ad00a651d15756aa054d084ef2348705.
[92] I. Herbert, Statistical analysis of copolymer sequence distribution, in: NMR Spectroscopy of Polymers, Springer, Dordrecht, 1993, https://doi.org/10.1007/978-94-011-2150-7_2.
[93] J.C. Randall, A review of high resolution liquid 13carbon nuclear magnetic resonance characterizations of ethylene-based polymers, J. Macromol. Sci., Part C 29 (2–3) (1989) 201–317, https://doi.org/10.1080/07366578908055172, arXiv:.
[94] K. Mezghani, P. Phillips, The $\gamma$-phase of high molecular weight isotactic polypropylene: iii. the equilibrium melting point and the phase diagram, Polymer 39 (16) (1998) 3735–3744. http://www.scopus.com/inward/record.uri?eid=2-s2.0-0032123021&partnerID=40&md5=56c9c2d8b13bcbf3a93058618607de64.
[95] C. Paulik, C. Tranninger, J. Wang, P. Shutov, D. Mileva, M. Gahleitner, Catalyst type effects on structure/property relations of polypropylene random copolymers,

arXiv: Macromol. Chem. Phys. 222 (23) (2021), 2100302 https://onlinelibrary.wiley.com/doi/pdf/10.1002/macp.202100302.

[96] J. Collette, D. Ovenall, W. Buck, R. Ferguson, Macromolecules 22 (10) (1989) 3858–3866, https://doi.org/10.1021/ma00200a007, cited By 91, https://www.scopus.com/inward/record.uri?eid=2-s2.0-0024749519&doi=10.1021%2fma00200a007&partnerID=40&md5=abf795fc828d31de3e7b6e9fe8bd032d.

[97] S. Cheng, J. Janimak, A. Zhang, E. Hsieh, Polymer 32 (4) (1991) 648–655, https://doi.org/10.1016/0032-3861(91)90477-Z, cited By 158, https://www.scopus.com/inward/record.uri?eid=2-s2.0-0026141489&doi=10.1016%2f0032-3861%2891%2990477-Z&partnerID=40&md5=15fa7daeb96b3d1da316dde8d0552a00.

[98] D. Mileva, R. Androsch, H.-J. Radusch, Polym. Bull. 61 (5) (2008) 643–654, https://doi.org/10.1007/s00289-008-0979-6, cited By 38, https://www.scopus.com/inward/record.uri?eid=2-s2.0-54949149490&doi=10.1007%2fs00289-008-0979-6&partnerID=40&md5=d2b3ea23c578632a0cff969e36062923.

[99] I. Sanchez, R. Eby, Macromolecules 8 (5) (1975) 638–641, https://doi.org/10.1021/ma60047a012, cited By 204, https://www.scopus.com/inward/record.uri?eid=2-s2.0-0001076583&doi=10.1021%2fma60047a012&partnerID=40&md5=f8c5cefe4d04c3d6371f2155038d796b.

[100] R. Kolb, C. Wutz, N. Stribeck, G. Von Krosigk, C. Riekel, Polymer 42 (12) (2001) 5257–5266, https://doi.org/10.1016/S0032-3861(00)00920-4, cited By 53, https://www.scopus.com/inward/record.uri?eid=2-s2.0-0035078158&doi=10.1016%2fS0032-3861%2800%2900920-4&partnerID=40&md5=ca29b66d7c5b87365a2a582f3073fbf3.

[101] J. Zhao, Y. Sun, Y. Men, Ind. Eng. Chem. Res. 56 (1) (2017) 198–205, https://doi.org/10.1021/acs.iecr.6b04087, cited By 8. doi: https://www.scopus.com/inward/record.uri?eid=2-s2.0-85017417560&doi=10.1021%2facs.iecr.6b04087&partnerID=40&md5=bee67e055b37ae9cd81b2c74643c1d96.

[102] D. Cavallo, L. Gardella, G. Alfonso, D. Mileva, R. Androsch, Polymer 53 (20) (2012) 4429–4437, https://doi.org/10.1016/j.polymer.2012.08.001, cited By 35, https://www.scopus.com/inward/record.uri?eid=2-s2.0-84865742254&doi=10.1016%2fj.polymer.2012.08.001&partnerID=40&md5=9c4cd40fa1b67a5940d6023e68a0c242.

[105] X. Guo, A.I. Isayev, M. Demiray, Crystallinity and microstructure in injection moldings of isotactic polypropylenes. part ii: simulation and experiment, arXiv: Polym. Eng. Sci. 39 (11) (1999) 2132–2149 https://onlinelibrary.wiley.com/doi/pdf/10.1002/pen.11603.